# ADRC-based dual-loop control and stability analysis of stacked interleaved DC–DC buck converter for hydrogen production using PEM electrolyzer

Nada Chhab, Abdelmajid Abouloifa, Elhoussin Elbouchikhi, Azeddine Houari, Ibtissam Lachkar

Energy Reports 15 (2026) 109154

Contents lists available at ScienceDirect

Energy Reports

journal homepage: www.elsevier.com/locate/egyr

Research paper

# ADRC-based dual-loop control and stability analysis of stacked interleaved DC–DC buck converter for hydrogen production using PEM electrolyzer

Nada Chhab [a,b,c], Abdelmajid Abouloifa [b], Elhoussin Elbouchikhi [d,*], Azeddine Houari [a], Ibtissam Lachkar [b]

[a] IREENA, Nantes University, Saint-Nazaire, France
[b] ESE Laboratory, ENSEM, Hassan II University, Casablanca, Morocco
[c] LABISEN, ISEN Yncrea Ouest, Nantes, France
[d] SATIE UMR CNRS 8029, CY Cergy-Paris University, Cergy-Pontoise, France

ARTICLE INFO

*Keywords:*
Hydrogen production
PEM electrolyzer
Active disturbance rejection control
Stability analysis

ABSTRACT

Hydrogen production via water electrolysis, particularly using Proton Exchange Membrane (PEM) electrolyzers, is a key technology for advancing renewable energy integration. Ensuring a stable and efficient supply requires DC–DC converters capable of precise regulation under disturbances. This paper proposes a dual-loop Active Disturbance Rejection Control (ADRC) strategy for a stacked interleaved DC–DC converter supplying a PEM electrolyzer. The proposed ADRC enhances robustness against disturbances and improves system stability under dynamic conditions typical of RES-based microgrids. Simulation results demonstrate that the approach significantly improves voltage regulation and overall performance—achieving a settling time of 10 ms and limiting overshoot to 20.06%—thereby ensuring a reliable and efficient power supply for PEM electrolyzers in renewable energy applications.

## 1. Introduction

Rapid industrialization and growing urbanization have led to a significant increase in global energy demand, even as fossil resources—historically the dominant energy sources—are gradually being depleted. This situation, coupled with rising environmental concerns, highlights the urgent need for a profound transformation of the global energy landscape. The energy transition cannot be limited to a mere technological substitution; it also requires overcoming the structural and institutional barriers resulting from a deep dependency on fossil-based infrastructures—a phenomenon referred to as carbon locking (Yang et al., 2024). Despite these inertias, some countries, particularly in the developing world, are demonstrating a growing commitment to initiating this shift. Ram et al. (2022) reports that in 2019, developing nations invested more than USD 152 billion in renewable energy, surpassing developed countries in relative terms to Gross Domestic Product.

However, the shift to an energy mix dominated by renewable sources presents new challenges, particularly due to their intermittent and unpredictable nature, this variability necessitates a transformation of current power networks into smart grids capable of dynamically adapting to fluctuations in generation and consumption (Khalid, 2024). In this context, energy storage systems (ESS) play a crucial role. ESS not only help stabilizing the grid and improving energy quality but also ensure a reliable power supply in the face of renewable intermittency (Elalfy et al., 2024). Their integration is therefore essential to the success of the energy transition.

Hydrogen, the most abundant gas in the universe, constitutes approximately 90% of visible matter and is distinguished by its energy density per unit weight (120 MJ/kg), significantly higher than fossil fuels, offering nearly three times the energy density of gasoline (Guilbert and Vitale, 2021). In this context, hydrogen energy storage emerges as a key solution for managing energy intermittency and optimizing renewable energy utilization. As shown in Fig. 1, hydrogen ESS integrated into a microgrid operates in three key stages (Bovo et al., 2023). First, it utilizes electrolysis to convert electrical energy from renewable sources into hydrogen and oxygen by splitting purified water. Next, the generated hydrogen is compressed and stored, while the oxygen is typically released into the atmosphere. Finally, during the energy conversion phase, the stored hydrogen is recombined with atmospheric oxygen in a fuel cell to generate electricity, with pure water as the only byproduct.

* Corresponding author.
*E-mail addresses:* nada.chhab@etu.univ-nantes.fr (N. Chhab), abdelmajid.abouloifa@univh2c.ma (A. Abouloifa), elhoussin.elbouchikhi@u-cergy.fr (E. Elbouchikhi), azeddine.houari@univ-nantes.fr (A. Houari), ibtissam.lachkar@univh2c.ma (I. Lachkar).

https://doi.org/10.1016/j.egyr.2026.109154
Received 21 August 2025; Received in revised form 26 February 2026; Accepted 3 March 2026
Available online 9 March 2026

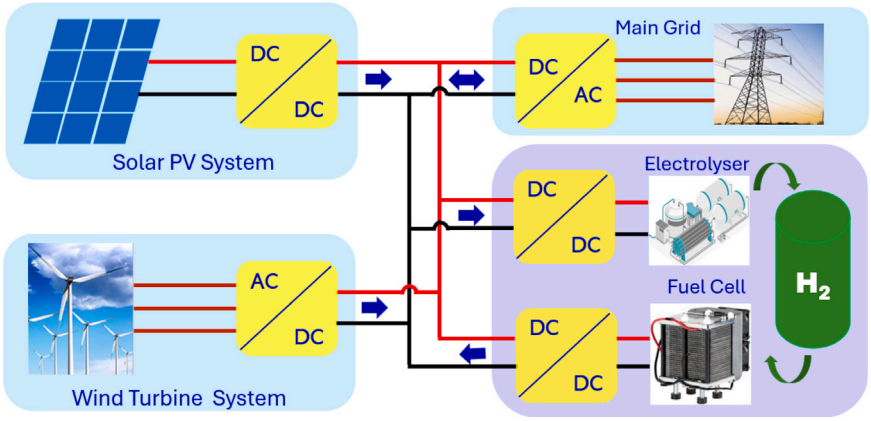


**Fig. 1.** Architecture of the renewable energy-based microgrid integrating a hydrogen storage system.

Beyond this functional scheme, recent literature emphasizes a sustainability-oriented reading of RES–electrolyzer–$H_2$ storage chains using established indicators: electrolysis energy intensity (ASEC, kWh $kg^{-1}$ $H_2$), electrical efficiency ($\eta_{el}$), levelized cost of hydrogen (LCOH, \$/kg $H_2$), and Life Cycle Assessment (LCA) metrics (e.g., Global Warming Potential (GWP)), all assessed at the system level including balance-of-plant. Reviews report typical ASEC values of 55–60 kWh/kg for low-temperature electrolyzers and 40–42 kWh/kg for high-temperature routes, with representative electrical efficiencies of about 57% and 77%, respectively, underscoring the need for integrated, system-level assessment (Franco and Giovannini, 2023). In RES-coupled operation, resource variability calls for the most stable possible supply: as an order of magnitude, the end-to-end PV→$H_2$ chain often achieves 8%–10% overall efficiency (approximately 330 kWh solar per kg $H_2$ under average conditions), which motivates robust control to limit off-MPP operation and associated losses (Franco and Giovannini, 2023). Techno-economic studies of HRES (PV + wind + electrolysis + $H_2$ storage) show strong site/resource dependence; for example, Dakhla (Morocco) reports LCOH ≈ 2.54 \$/kg, whereas Poland reports 6.37–13.48 \$/kg depending on location and pathway, while Power-to-Gas architectures aid curtailment management and sector coupling, reinforcing system-level sustainability (Nnabuife et al., 2025).

Among electrolysis technologies, PEM technology has several advantages, including compactness, high current density, and energy efficiency. However, the high costs of catalysts such as platinum and iridium remain a significant challenge (Kumar and Himabindu, 2019). In this context, the electric energy generated by renewable energy sources (RES) cannot be directly used for hydrogen production, as the DC bus voltage provided by RES systems is significantly higher than the operating voltage of an electrolyzer. Therefore, a power converter is essential to properly interface the energy source and the electrolyzer (Yue et al., 2021), Abdel-Rahim et al. (2024). To guarantee a stable and efficient operation of electrolyzers in hydrogen production systems powered by RES, several critical factors must be considered. These include low-voltage, high-current operation, minimizing output current ripple to improve energy efficiency, and ensuring high reliability in the event of power switch failures, which is crucial for maintaining a consistent hydrogen production rate and extending the electrolyzer's lifespan (Guo et al., 2022).

DC–DC converters are generally classified into isolated and non-isolated types. Isolated converters provide galvanic isolation, which guarantees safety but comes with drawbacks such as leakage inductance, core saturation, and larger size, making them more expensive (Greco et al., 2017; Mumtaz et al., 2021). In contrast, non-isolated converters are favored for their simpler design, lower cost, and compactness (Al-Obaidi et al., 2022). Among these, the buck converter is commonly used, but conventional implementations suffer from high voltage stress and large output current ripples, which increase losses and reduce efficiency (Farooq et al., 2015). These limitations make them unsuitable for high step-down applications such as electrolyzers, which require very low output voltages compared to typical renewable energy sources (Yodwong et al., 2024). To address these issues, interleaved buck converter topologies have been developed, reducing current ripples and increasing power capacity by operating multiple converters in parallel (Farooq et al., 2015). Interleaved converters offer significant advantages over conventional topologies and are therefore increasingly adopted in various application domains. In battery energy storage systems, Kumar and Nagendrappa (2023) report a bidirectional DC–DC converter enabling power transfer with improved efficiency, reduced size, and lower input-source ripple compared with conventional buck–boost structures. In proton exchange membrane fuel-cell systems, Cao et al. (2020) integrate a two-phase interleaved DC–DC converter to increase the terminal output voltage and to help maintain the PEMFC at a desired operating point under current variations. For electrified transportation, Melo et al. (2020) highlight the role of an interleaved bidirectional DC–DC converter interfacing batteries and supercapacitors through a DC link, providing high efficiency over a wide load range and suitability for high-power/high-current levels. In grid-connected photovoltaic applications, Marish Kumar et al. (2024) combine an interleaved boost converter with a three-level NPC inverter to enhance energy harvesting efficiency in PV systems.

Hydrogen production by water electrolysis consists of a converter supplying the electrolyzer. This energy conversion system can be subjected to internal and external disturbances. Moreover, several uncertainties need to be taken into account during modeling and control process. For example, the internal parameters of the electrolyzer can be significantly affected by variations in temperature and pressure, which influence performance and stability.

Numerous recent studies have focused on the design and control of DC–DC converters dedicated to powering electrolyzers in green hydrogen production systems, in response to increasing demands for reliability, energy efficiency, current ripple reduction, and fault tolerance. In Yodwong et al. (2023), an innovative fault diagnosis method is developed to detect and locate open-circuit faults in a three-level interleaved buck converter while ensuring fault-tolerant control without hardware redundancy. The work presented in Concha et al. (2024) proposes a high-power converter topology with phase-shift control, suitable for PEM electrolyzers powered through a medium-voltage DC bus grid, targeting ripple reduction and improved reliability. In Concha et al. (2024), an original control strategy is implemented in a three-channel interleaved dual buck converter, ensuring both current regulation for the electrolyzer and input capacitor voltage balancing. Study (Zhao et al., 2023) combines a nonlinear electrochemical model of an alkaline electrolyzer with an active front and phase shifted full bridge converter in a co-simulation framework, enabling optimized controller design and compliance with grid requirements. Finally, study (Guo et al., 2022)

introduces an improved topology of a stacked multiphase interleaved buck converter, accompanied by a generalized modulation method and two fault-tolerant control strategies, allowing flexible, robust, and efficient operation of electrolyzers in renewable-energy-based hydrogen production.

In the literature, several studies have addressed this issue and proposed various control strategies to mitigate these uncertainties and disturbances. For instance, Koundi et al. (2019) proposes an approach based on an output feedback controller, combining an observer and a sliding mode control. Similarly, Koundi et al. (2022) implements an adaptive output feedback control, integrating an adaptive observer based on an extended Kalman filter and a super-twisting sliding mode controller to enhance system robustness. Meanwhile, Baraean et al. (2024) employs a combination of adaptive backstepping terminal sliding mode control and a Physics-Informed Neural Network to estimate and compensate for system uncertainties. Finally, Makineni et al. (2025) adopts an integral sliding mode control approach, enabling the compensation of both matched and unmatched uncertainties and disturbances.

Active Disturbance Rejection Control (ADRC), developed in Han (2009), represents a major advancement in the field of control systems. Unlike traditional methods, ADRC relies on minimal system knowledge, such as its order and an approximation of certain parameters, making it particularly robust and adaptable. This paradigm transforms complex dynamics into stable and linear behaviors through the direct rejection of generalized disturbances, thus marking a departure from conventional approaches (Gao, 2006).

ADRC has been successfully applied in several domains requiring robust disturbance rejection. In power electronics, Ma et al. (2019) report improved regulation and smooth response to load disturbances for a proton exchange membrane fuel cell DC–DC converter using ADRC. In thermal power plants, Sun et al. (2017) show that replacing the outer-loop PI controller by ADRC improves the control of superheater steam temperature under wide load variations. For autonomous flight, Shen and Xu (2021) use a radial basis function neural network combined with ADRC to enhance unmanned helicopter trajectory tracking under unknown disturbances. In autonomous ground vehicles, Wu et al. (2019) demonstrate that ADRC improves path-following performance by estimating and compensating unmodeled dynamics and external perturbations in real time. Similarly, Castañeda et al. (2015) confirm the suitability of ADRC for nonlinear trajectory tracking problems with strong anti-disturbance capability. However, the nonlinear version of ADRC (NLADRC), while effective in handling uncertainties and improving system dynamics, presents drawbacks related to its complexity and the need for meticulous tuning of numerous parameters (Li et al., 2017). To overcome these limitations, Gao (2003) introduced a linear version (LADRC) in 2003, linearizing all components of ADRC to enable simplified stability analysis and enhanced practicality. This approach is based on bandwidth parameterization, where only two parameters, the controller bandwidth and the observer bandwidth, need to be adjusted. This confers a clear advantage on LADRC in terms of simplicity of tuning and theoretical analysis (Li et al., 2017). Recent studies confirm the potential of ADRC to improve voltage regulation and robustness in power electronic systems (Wang et al., 2023), which motivates its application in electrolyzer supply control explored in this work.

The main contributions of this paper can be summarized as follows:

- A cascaded Active Disturbance Rejection Control (ADRC) strategy is proposed for a stacked interleaved buck converter supplying a PEM electrolyzer.
- The control scheme is explicitly designed to address system-specific challenges such as strong external disturbances, thermal sensitivity of electrolyzer parameters, and the requirement for accurate voltage regulation under low-voltage and high-current operating conditions.
- Extended State Observers (ESOs) are incorporated within both the inner current loop and the outer voltage loop, enabling real-time estimation and rejection of generalized disturbances. The cascaded control structure significantly improves robustness, transient performance, and flexible voltage adaptation to dynamic operating conditions of the electrolyzer.
- A rigorous theoretical stability analysis is conducted, establishing formal guarantees of robustness and convergence for the closed-loop system.

The remainder of this paper is organized as follows. Section 2 presents the modeling of the Proton Exchange Membrane (PEM) electrolyzer, covering both static and dynamic aspects. Section 3 describes the modeling of the Stacked Interleaved Buck Converter (SIBC), the design of the proposed ADRC-based control strategy, and the associated stability analysis. Section 4 discusses the simulation results that validate the performance and robustness of the proposed approach. Finally, Section 5 concludes the paper and outlines future research directions.

## 2. Proton exchange membrane electrolyzer

A PEM electrolyzer, initially developed by General Electric in the 1960s to overcome the limitations of Alkaline Electrolyzers (Kumar and Himabindu, 2019), is an electrochemical device that directly converts electrical energy into chemical energy by splitting water into hydrogen and oxygen. This process relies on a proton-conducting membrane (proton exchange membrane) used as the electrolyte.

The operation of the PEMEL is based on two main reactions:

- Oxidation reaction at the anode: Under the effect of an applied electrical voltage, water is split in the anode catalyst layer into protons ($H^+$), electrons ($e^-$), and oxygen ($O_2$).
- Reduction reaction at the cathode: Protons travel through the proton-conducting membrane to the cathode, where they combine with electrons from the external circuit to form hydrogen ($H_2$).

### 2.1. Static modeling

The static model of a PEM electrolyzer (PEM EL) can be mathematically described by (1), which expresses the cell voltage as the sum of the reversible voltage and several types of overvoltages, including ohmic and activation overvoltages at both the anode and cathode.

$$V_{\text{cell}} = E_{\text{rev}} + V_{\text{ohm}} + V_{\text{act}} + V_{\text{diff}} \tag{1}$$

#### 2.1.1. Reversible potential

The reversible potential is the minimum potential level required to initiate the dissociation of water between the electrodes of an electrolysis cell. It consists of two terms: $E^0_{\text{rev}}$, the reversible voltage under standard conditions and a second term accounting for deviations from these conditions. The value of $E^0_{\text{rev}}$ is often set to 1.299 V under standard conditions (P = 1 atm, T = 298.15 K), but it decreases with increasing temperature, described by various empirical equations (Marefatjouikilevaee et al., 2023).

$$E_{\text{rev}} = E^0_{\text{rev}} + \frac{RT_{\text{cell}}}{2F} \ln\left(\frac{P_{H_2} + P^{0.5}_{O_2}}{P_0}\right) \tag{2}$$

$$E^0_{\text{rev}} = \frac{\Delta G^0}{nF} \tag{3}$$

where $F$ is the Faraday constant, $E^0_{\text{rev}}$ is the reversible voltage under standard conditions, $R$ is the universal gas constant, $P_{H_2}$ is the hydrogen pressure, $P_{O_2}$ is the oxygen pressure, $P_0$ is the reference pressure, $n$ is the number of electrons transferred in the chemical reaction ($n = 2$), $T_{cell}$ is the cell temperature and $\Delta G^0$ is the Gibbs free energy under standard conditions.

#### 2.1.2. Activation overpotential

Activation overpotential is the excess voltage required to drive electrochemical kinetics during electron charge transfer reactions at the electrodes. It depends on catalyst materials, catalyst active surface area, and temperature. It is described by the Butler–Volmer Eq. (4) or the Tafel correlation (5) (Koundi et al., 2023):

$$V_{\text{act}} = \frac{RT}{\alpha_{\text{an}} F} \sinh^{-1}\left(\frac{j_{\text{an}}}{2j_{0,\text{an}}}\right) + \frac{RT}{\alpha_{\text{cat}} F} \sinh^{-1}\left(\frac{j_{\text{cat}}}{2j_{0,\text{cat}}}\right) \tag{4}$$

$$V_{\text{act}} = \frac{RT}{2\alpha_{\text{an}} F} \ln\left(\frac{j_{\text{an}}}{j_{0,\text{an}}}\right) + \frac{RT}{2\alpha_{\text{cat}} F} \ln\left(\frac{j_{\text{cat}}}{j_{0,\text{cat}}}\right) \tag{5}$$

where $\alpha_{\text{an}}$ and $\alpha_{\text{cat}}$ are the charge transfer coefficients at the anode and cathode, respectively, $j_{\text{an}}$ and $j_{\text{cat}}$ are the current densities of the electrodes, $j_{0,\text{an}}$ and $j_{0,\text{cat}}$ are the exchange current densities of the electrodes.

#### 2.1.3. Ohmic overpotential

As indicated in (6), the ohmic overpotential $V_{\text{ohm}}$ in the cell are due to two components: the electronic resistance $R_{\text{ele}}$ caused by the materials of the electrodes and bipolar plates, as well as the ionic resistance of the membrane $R_{\text{mem}}$, which is related to ion transport through the membrane (Koundi et al., 2023).

$$V_{\text{ohm}} = R_{\text{ohm}} I_{\text{cell}} = (R_{\text{mem}} + R_{\text{ele}}) I_{\text{cell}} \tag{6}$$

where $R_{mem}$ and $R_{ele}$ are given by

$$R_{\text{mem}} = \frac{\delta_{\text{mem}}}{A_{\text{mem}} \sigma_{\text{mem}}} \qquad R_{\text{ele}} = \frac{\phi_{\text{ele}} l_{\text{ele}}}{A_{\text{ele}}} \tag{7}$$

$\delta_{\text{mem}}$ is the membrane thickness, $A_{\text{mem}}$ is the membrane surface area, and $\sigma_{\text{mem}}$ is the membrane conductivity and $\phi_{\text{ele}}$ represents the material resistivity, $l_{\text{ele}}$ is the electron path length, and $A_{\text{ele}}$ denotes the conductor cross-sectional area.

#### 2.1.4. Diffusion overpotential

The diffusion overpotential is the additional voltage required to sustain an electrochemical reaction at high current densities, due to the limitation of reactant transport to the electrodes or product transport away from the electrodes (Marefatjouikilevaee et al., 2023).

$$V_{\text{diff}} = \frac{RT}{\beta n F} \ln\left(1 - \frac{j_{\text{cell}}}{j_{\text{lim}}}\right) \tag{8}$$

where $\beta$ is the diffusion coefficient and $j_{\text{lim}}$ is the limiting current density for the diffusion of liquid water.

### 2.2. Dynamic modeling of the PEM electrolyzer

Fig. 2 illustrates the dynamic equivalent electrical model of the PEM electrolyzer used in the simulations carried out in this study (Ratib et al., 2025), the corresponding electrical characteristics and model parameters are summarized in Table 1. This model includes:

- A DC voltage source representing the reversible voltage $E_{\text{rev}}$.
- A series resistance $R_{\text{ohm}}$ accounting for ohmic losses.
- Two parallel RC branches connected in series, composed of $C_{\text{a}}$, $R_{\text{a}}$ for the anode and $C_{\text{c}}$, $R_{\text{c}}$ for the cathode, to simulate the capacitive and resistive properties of each electrode.

These parallel RC circuits are used to model the double-layer capacitance as well as the voltage losses related to activation and concentration phenomena occurring during the water electrolysis process. In electrochemical systems, the formation of the double-layer is mainly attributed to diffusion phenomena resulting from the interaction between the electrons of the electrodes and the ions in the electrolyte. Moreover, this phenomenon is also influenced by the application of external voltages.

**Table 1**
Electrical characteristics and parameters of the PEM electrolyzer equivalent model.

| Parameter | Value |
|---|---|
| Nominal Input Voltage | 750 V |
| Standard Reversible Cell Voltage | 4.8 V |
| Anode Ohmic Resistance | 1.47 Ω |
| Cathode Ohmic Resistance | 0.147 Ω |
| Membrane Ohmic Resistance | 1.616 Ω |
| Equivalent Parallel Capacitance | 18.63 F |

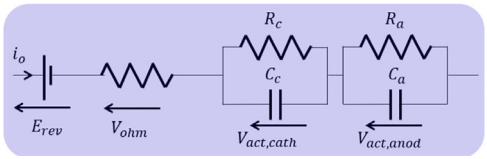


**Fig. 2.** The dynamic electrical model of the PEM electrolyzer.

## 3. Stacked interleaved buck converter modeling, control, and stability analysis

The *stacked interleaved* topology was designed to overcome the limitations of classical *interleaved* configurations, which are highly dependent on the duty cycle and require a large number of phases to fully cancel current ripple. In traditional approaches, this complete cancellation is only possible at specific duty cycles, which limits their performance and overall efficiency. Additionally, adding more phases increases both the system size and complexity. By eliminating this dependency on the duty cycle and reducing the number of phases required to just two, the *stacked interleaved* topology offers an optimized solution. It is specifically designed to utilize on-chip components, such as inductors and capacitors, thus providing improved compactness and enhanced energy efficiency (Guida et al., 2018). Due to its numerous advantages, this topology has been subsequently used to power PEM electrolyzers as shown in Fig. 3, perfectly meeting the requirements of these systems in terms of reliability and performance. The operation of the converter, as illustrated in Fig. 4, is organized as follows:

- **Primary phase**: The power switches $\overline{\mu}$, associated with the components $L_p$, $R_p$, and $C_p$, are connected to the load and operate with a duty cycle of $1 - u$.
- **Secondary phase**: The power switches $\mu$, associated with the components $L_s$, $R_s$, and $C_s$, are not connected to the load and operate with a duty cycle of $u$.

Due to this configuration, the two phases generate different voltages. Coupling the two phases with the capacitor $C_s$ enables the generation of these distinct voltages while simultaneously canceling the current ripple at the converter's output.

### 3.1. System modeling

The average model of the stacked interleaved buck converter (SIBC) supplying the PEM electrolyzer is derived using Kirchhoff's voltage and current laws, and is expressed by the set of fourth-order differential equations (9)–(12). In this formulation, $\bar{v}_p$ denotes the average output voltage across the primary capacitor, while $\bar{i}_p$ and $\bar{i}_s$ represent the primary and secondary inductor currents, respectively. The variable $\bar{v}_s$ corresponds to the secondary capacitor voltage. The circuit parameters include the inductances $L_p$ and $L_s$ with their equivalent resistances $R_p$ and $R_s$, as well as the primary and secondary capacitances $C_p$ and $C_s$. The electrolyzer dynamics are incorporated through its reversible voltage $E_{rev}$, the activation overvoltages $V_{cath}$ and $V_{anod}$, and the ohmic resistance $R_{ohm}$. The input voltage source is represented by $E$, while

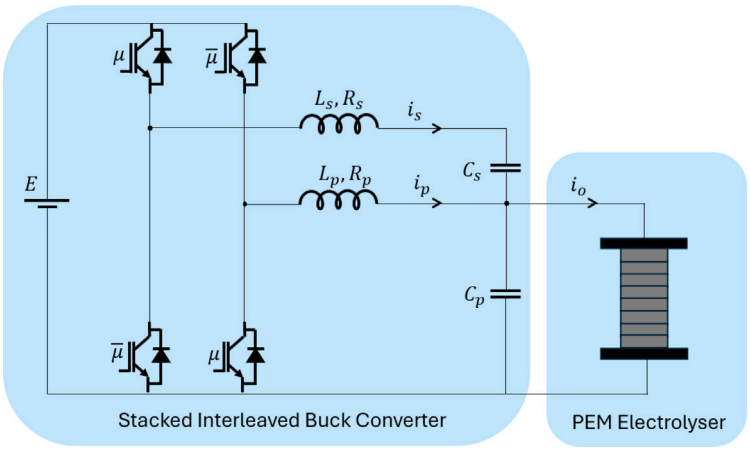


**Fig. 3.** Schematic circuit diagram of the SIBC supplying the PEM electrolyzer.

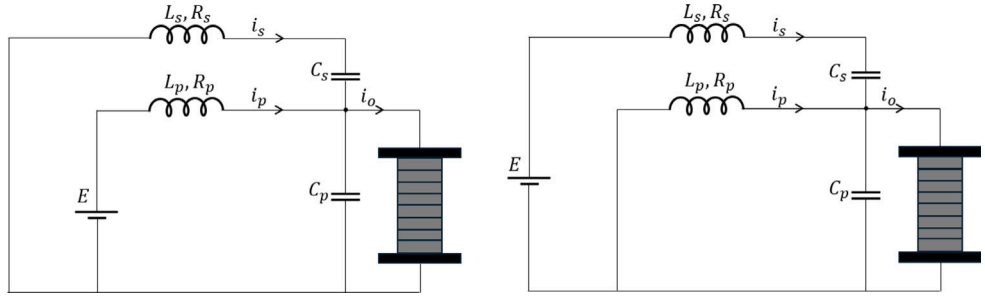


**Fig. 4.** Schematic circuit diagram of the two operating modes of the overall system (SIBC and PEM electrolyzer).

the duty cycle $u$ defines the control action. This averaged fourth-order model, obtained from fundamental circuit laws, captures the essential dynamics of the converter–electrolyzer interaction and establishes the foundation for the subsequent controller design and stability analysis.

$$\frac{d\bar{v}_p}{dt} = \frac{1}{C_p}\bar{i}_s + \frac{1}{C_p}\bar{i}_p + \frac{\left(-\bar{v}_p + E_{\text{rev}} + V_{\text{cath}} + V_{\text{anod}}\right)}{C_p R_{\text{ohm}}} \tag{9}$$

$$\frac{d\bar{i}_p}{dt} = -\frac{R_p}{L_p}\bar{i}_p - \frac{1}{L_p}\bar{v}_p + \frac{E}{L_p} - \frac{E}{L_p}u \tag{10}$$

$$\frac{d\bar{i}_s}{dt} = -\frac{R_s}{L_s}\bar{i}_s - \frac{1}{L_s}\bar{v}_p - \frac{1}{L_s}\bar{v}_s + \frac{E}{L_s}u \tag{11}$$

$$\frac{d\bar{v}_s}{dt} = \frac{1}{C_s}\bar{i}_s \tag{12}$$

### 3.2. Regulator structure

The objective of the control strategy is to regulate the electrolyzer voltage around a desired reference value. The controller adopts a cascade architecture, where the inner loop is responsible for tracking the current reference $i_p^*$ by adjusting the converter's duty cycle. Notably, the average current drawn by the electrolyzer closely follows the current $\bar{i}_p$ provided that the average of $\bar{i}_s$ remains zero. The outer loop manages the regulation of the voltage $\bar{v}_p$ by generating the intermediate control signal $i_p^*$. To ensure the effectiveness of the overall control system, the inner loop must exhibit a dynamic response that is significantly faster than that of the outer loop. To fulfill all of these objectives, a controller based on the ADRC approach has been developed

### 3.3. Active disturbance rejection control

The ADRC provides a control method that considerably minimizes the reliance on explicit modeling. The approach allows actively estimate the perturbation $f$ and then neutralize it in real-time. The problem is thus simplified to the control of an integrator-type system. Three essential components are required: a tracking differentiator, an extended state observer and a linear state error feedback. To implement ADRC, it is necessary to represent the system in the form of a state–space model, defined as follows:

$$\begin{cases} \dot{x}_1 = x_2 \\ \dot{x}_2 = x_3 \\ \vdots \\ \dot{x}_{n-1} = f + bu \\ \dot{x}_n = \dot{f} \\ y = x_1 \end{cases} \tag{13}$$

Fig. 5 illustrates the general structure of the proposed cascaded control strategy. This architecture consists of two control loops: an outer voltage control loop and an inner current control loop. In this structure, the blocks denoted as $F_o$ and $F_i$ represent the Tracking Differentiators, which are used to smooth sudden variations in the input reference and to generate a filtered derivative reference signal. In this work, a low-pass filter was used to perform this function in order to simplify the implementation.

The blocks $ESO_o$ and $ESO_i$ correspond to the Extended State Observers, which constitute a key component of the ADRC strategy. Their role is to estimate both the internal states of the system and the total disturbances or uncertainties acting on it.

Finally, the blocks $R_o$ and $R_i$ represent the controllers used in each control loop. These controllers combine a conventional linear control law with active disturbance compensation, ensuring accurate reference tracking and good robustness against system uncertainties.

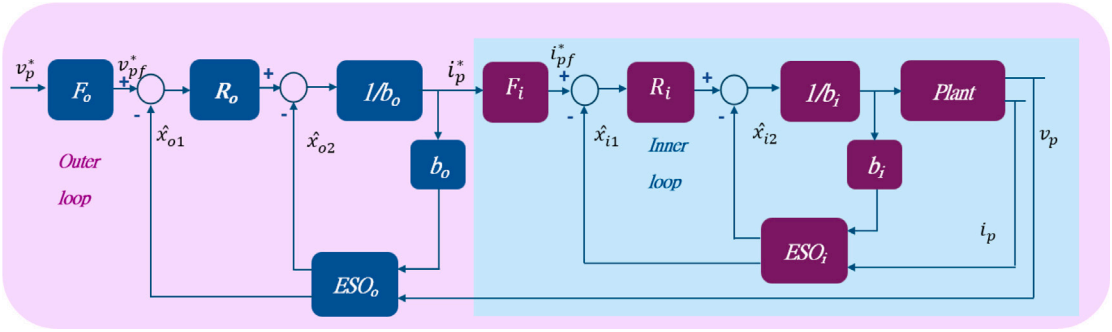


**Fig. 5.** General structure of the proposed cascade control strategy.

### 3.3.1. Current inner-loop design

The controller is synthesized using the ADRC approach, based on the current dynamics described by the following differential equation:

$$\frac{d\bar{i}_p}{dt} = -\frac{R_p}{L_p}\bar{i}_p - \frac{1}{L_p}\bar{v}_p + \frac{E}{L_p} - \frac{E}{L_p}u \tag{14}$$

This model can be written in the following suitable form:

$$\dot{x}_{i1} = f_i + b_i u \tag{15}$$

where

$$f_i = -\frac{R_p}{L_p}\bar{i}_p - \frac{1}{L_p}\bar{v}_p + \frac{E}{L_p} \tag{16}$$

$$b_i = -\frac{E}{L_p} \tag{17}$$

### 3.3.2. Extended state observer design

To obtain $f_i$, we extend the state vector to include it as an additional state. In other words, we define

$$x_i = \begin{pmatrix} x_{i1} & x_{i2} \end{pmatrix}^T = \begin{pmatrix} x_{i1} & f_i \end{pmatrix}^T \tag{18}$$

The system state model (10) then becomes:

$$\begin{pmatrix} \dot{x}_{i1} \\ \dot{x}_{i2} \end{pmatrix} = \begin{pmatrix} 0 & 1 \\ 0 & 0 \end{pmatrix} \begin{pmatrix} x_{i1} \\ x_{i2} \end{pmatrix} + \begin{pmatrix} b_i \\ 0 \end{pmatrix} u + \begin{pmatrix} 0 \\ 1 \end{pmatrix} \frac{df_i}{dt} \tag{19}$$

On the basis of the last model, an ESO is built:

$$\begin{pmatrix} \dot{\hat{x}}_{i1} \\ \dot{\hat{x}}_{i2} \end{pmatrix} = \begin{pmatrix} 0 & 1 \\ 0 & 0 \end{pmatrix} \begin{pmatrix} \hat{x}_{i1} \\ \hat{x}_{i2} \end{pmatrix} + \begin{pmatrix} b_i \\ 0 \end{pmatrix} u + \begin{pmatrix} 2\omega_i \\ \omega_i^2 \end{pmatrix} (x_{i1} - \hat{x}_{i1}) \tag{20}$$

The observer in (20) can be expressed in the following suitable form:

$$\begin{pmatrix} \dot{\hat{x}}_{i1} \\ \dot{\hat{x}}_{i2} \end{pmatrix} = \begin{pmatrix} -2\omega_i & 1 \\ -\omega_i^2 & 0 \end{pmatrix} \begin{pmatrix} \hat{x}_{i1} \\ \hat{x}_{i2} \end{pmatrix} + \begin{pmatrix} b_i \\ 0 \end{pmatrix} u + \begin{pmatrix} 2\omega_i \\ \omega_i^2 \end{pmatrix} x_{i1} \tag{21}$$

The bandwidth $\omega_i$ is the only adjustment parameter determining the observer's dynamic behavior. As a result, the latter has a double pole at $-\omega_i$.

Subtracting (20) from (19), the error dynamics of the $ESO_i$ is as follows:

$$\begin{pmatrix} \dot{\tilde{x}}_{i1} \\ \dot{\tilde{x}}_{i2} \end{pmatrix} = \begin{pmatrix} -2\omega_i & 1 \\ -\omega_i^2 & 0 \end{pmatrix} \begin{pmatrix} \tilde{x}_{i1} \\ \tilde{x}_{i2} \end{pmatrix} + \begin{pmatrix} 0 \\ 1 \end{pmatrix} \frac{df_i}{dt} \tag{22}$$

### 3.3.3. Linear state error feedback design

The control law is designed as

$$u_i = \frac{1}{b_i}(-\hat{x}_{i2} + v) \tag{23}$$

The previous control law reduces the plant (11) to the following approximate first-order integral plant:

$$\dot{x}_{i1} = \tilde{x}_{i2} + v \tag{24}$$

which can be governed by the following control law

$$v = k_i(i_{pf}^* - \hat{x}_{i1}) \tag{25}$$

Finally, the closed-loop system is described by:

$$\dot{x}_{i1} = \tilde{x}_{i2} + k_i(i_{pf}^* - \hat{x}_{i1}) \tag{26}$$

If we define the tracking error as:

$$e_i = \begin{pmatrix} e_{i1} \\ e_{i2} \end{pmatrix} = \begin{pmatrix} x_{i1} - i_{pf}^* \\ i_{pf}^* - i_p^* \end{pmatrix} \tag{27}$$

Then

$$\dot{e}_{i1} = k_i\tilde{x}_{i1} + \tilde{x}_{i2} - k_i e_{i1} + \frac{1}{T_i}e_{i2} \tag{28}$$

$$\dot{e}_{i2} = -\frac{1}{T_i}e_{i2} - \frac{di_p^*}{dt} \tag{29}$$

### 3.3.4. Voltage outer-loop design

The synthesis of the regulator for the external loop will also be developed using the ADRC approach, based on the dynamics of the electrolyzer voltage (9), assuming that the internal loop is sufficiently fast and operates correctly. The model (9) can be written in the following suitable form:

$$\dot{x}_{o1} = f_o + b_o i_p^* \tag{30}$$

where $f_o$ and $b_o$ are given by:

$$f_o = \frac{1}{C_p}\bar{i}_s + \frac{\left(-\bar{v}_p + E_{\text{rev}} + V_{\text{cath}} + V_{\text{anod}}\right)}{C_p R_{\text{ohm}}} \tag{31}$$

$$b_o = \frac{1}{C_p}\bar{i}_p \tag{32}$$

As with the internal current loop, we extend the state vector to include $f_o$ as an additional state. In other words, we define:

$$x_o = \begin{pmatrix} x_{o1} & x_{o2} \end{pmatrix}^T = \begin{pmatrix} x_{o1} & f_o \end{pmatrix}^T \tag{33}$$

The system (30) can be expressed in the following form:

$$\begin{pmatrix} \dot{x}_{o1} \\ \dot{x}_{o2} \end{pmatrix} = \begin{pmatrix} 0 & 1 \\ 0 & 0 \end{pmatrix} \begin{pmatrix} x_{o1} \\ x_{o2} \end{pmatrix} + \begin{pmatrix} b_o \\ 0 \end{pmatrix} u + \begin{pmatrix} 0 \\ 1 \end{pmatrix} \frac{df_o}{dt} \tag{34}$$

This model suggests the extended state observer ($ESO_o$) given in (35) and the control law ($R_o$) shown in (36):

$$\begin{pmatrix} \dot{\hat{x}}_{o1} \\ \dot{\hat{x}}_{o2} \end{pmatrix} = \begin{pmatrix} -2\omega_o & 1 \\ -\omega_o^2 & 0 \end{pmatrix} \begin{pmatrix} \hat{x}_{o1} \\ \hat{x}_{o2} \end{pmatrix} + \begin{pmatrix} b_o \\ 0 \end{pmatrix} u + \begin{pmatrix} 2\omega_o \\ \omega_o^2 \end{pmatrix} x_{o1} \tag{35}$$

$$i_p^* = k_o(v_{pf}^* - \hat{x}_{o1}) \tag{36}$$

The dynamics of the closed-loop system then become:

$$\dot{x}_{o1} = \tilde{x}_{o2} + k_o(v_{pf}^* - \hat{x}_{io}) \tag{37}$$

Note that the tuning parameters $\omega_o$ and $k_o$ set the dynamics of the observer and the regulator, respectively. Furthermore, the observation error is given by:

$$\begin{pmatrix} \dot{\tilde{x}}_{o1} \\ \dot{\tilde{x}}_{o2} \end{pmatrix} = \begin{pmatrix} -2\omega_o & 1 \\ -\omega_o^2 & 0 \end{pmatrix} \begin{pmatrix} \tilde{x}_{o1} \\ \tilde{x}_{o2} \end{pmatrix} + \begin{pmatrix} 0 \\ 1 \end{pmatrix} \frac{df_o}{dt} \tag{38}$$

Finally, the closed-loop system is described by:

$$\dot{x}_{o1} = \tilde{x}_{o2} + k_o(v_{pf}^* - \hat{x}_{o1}) \tag{39}$$

If we define the following tracking errors:

$$e_o = \begin{pmatrix} e_{o1} \\ e_{o2} \end{pmatrix} = \begin{pmatrix} x_{o1} - v_{pf}^* \\ v_{pf}^* - v_p^* \end{pmatrix} \tag{40}$$

Then,

$$\dot{e}_{o1} = k_o\tilde{x}_{o1} + \tilde{x}_{o2} - k_o e_{o1} + \frac{1}{T_o}e_{o2} \tag{41}$$

$$\dot{e}_{o2} = -\frac{1}{T_o}e_{o2} - \frac{dv_p^*}{dt} \tag{42}$$

**Remark:**

$$\frac{di_p^*}{dt} = -k_o(k_o + 2\omega_o)\tilde{x}_{o1} + k_o^2 e_{o1} - \frac{k_o}{T_o}e_{o2} \tag{43}$$

### 3.4. Stability analysis

This section aims to establish the stability of the overall system, which includes the electrolyzer powered by an SIBC and controlled using an ADRC approach with both internal and external loops. Previous research (Zhang et al., 2018) has shown that the estimation error of the ESO and the tracking error of the ADRC-controlled closed-loop system are uniformly ultimately bounded, decreasing steadily as their respective bandwidths increase. This demonstrates the stability of the ADRC system, utilizing the converse Lyapunov theorem and disturbance theory. Additionally, the stability of ADRC in time-varying systems has been analyzed using the singular perturbation method (Zhou et al., 2009), which divides the system's dynamics into slow and fast subsystems. This technique provides a framework for proving exponential stability and establishing a lower bound for the observer bandwidth. These studies offer a solid foundation for analyzing the stability of the ADRC-controlled system in the present work.

Using the dynamic expressions derived in (22), (28), (29), (36), (41), (42), and (43), the overall system's behavior, expressed in terms of the error coordinates,

$$Z = \begin{pmatrix} \tilde{x}_{i1} & \tilde{x}_{i2} & e_{i1} & e_{i2} & \tilde{x}_{o1} & \tilde{x}_{o2} & e_{o1} & e_{o2} \end{pmatrix}^T,$$

can be described as follows:

$$\dot{Z} = AZ + B\frac{d}{dt}\Gamma \tag{44}$$

where $A$ is given by

$$A = \begin{pmatrix} A_{11} & A_{12} \\ A_{21} & A_{22} \end{pmatrix} \tag{45}$$

and $A_{11}$, $A_{12}$, $A_{21}$, $A_{22}$ and $B$ are

$$A_{11} = \begin{pmatrix} -2\omega_i & -\omega_i^2 & k_i & 0 \\ 1 & 0 & 1 & 0 \\ 0 & 0 & -k_i & 0 \\ 0 & 0 & \frac{1}{T_i} & -\frac{1}{T_i} \end{pmatrix} \tag{46}$$

$$A_{12} = \begin{pmatrix} \mathbf{0}_{4\times4} \end{pmatrix} \tag{47}$$

$$A_{21} = \begin{pmatrix} 0 & 0 & 0 & k_o(k_o + 2\omega_o) \\ 0 & 0 & 0 & 0 \\ 0 & 0 & 0 & 0 \\ 0 & 0 & -k_o^2 & \frac{k_o}{T_o} \end{pmatrix} \tag{48}$$

$$A_{22} = \begin{pmatrix} -2\omega_o & -\omega_o^2 & k_o & 0 \\ 1 & 0 & 1 & 0 \\ 0 & 0 & -k_o & 0 \\ 0 & 0 & \frac{1}{T_o} & -\frac{1}{T_o} \end{pmatrix} \tag{49}$$

$$B = \begin{pmatrix} B_1 \\ B_2 \end{pmatrix} \tag{50}$$

where $B_1$, $B_2$ and $\Gamma$ are:

$$B_1 = \begin{pmatrix} 0 & 1 & 0 \\ 0 & 0 & 0 \\ 0 & 0 & 0 \\ 0 & 0 & -1 \end{pmatrix} \tag{51}$$

$$B_2 = \begin{pmatrix} \mathbf{0}_{4\times4} \end{pmatrix} \tag{52}$$

$$\Gamma = \begin{pmatrix} f_i(t) \\ f_o(t) \\ v_p^* \end{pmatrix} \tag{53}$$

**Theorem.** Consider the system consisting of the converter–electrolyzer combination depicted in Fig. 2, represented by its averaged model (9)–(12) and controlled by the current and voltage loops described above. Under the practical assumption that the components of the vector $\Gamma$ asymptotically tend toward constant values, the closed-loop system is exponentially stable if and only if the matrix $A$ is Hurwitz.

**Proof.** The characteristic polynomial of the matrix $A$ is given by:

$$\begin{aligned} |sI - A| =& (s + \frac{1}{T_o})(s + k_i)(s + k_o) \\ & (s^2 + 2\omega_o s + \omega_o^2)(s + \frac{1}{T_i})(s + k_i) \\ & (s^2 + 2\omega_i s + \omega_i^2) \end{aligned} \tag{54}$$

From this expression, we can identify the roots of the characteristic polynomial:

i. A double pole at $-\omega_i$ related to the extended observer of the internal current loop.

ii. A simple pole at $-k_i$ introduced by the internal loop controller.

iii. A simple pole at $-\frac{1}{T_i}$ brought by the smoothing filter of the internal loop reference signal.

iv. A double pole at $-\omega_o$ associated with the extended observer of the external voltage loop.

v. A simple pole at $-k_o$ introduced by the external loop controller.

vi. A simple pole at $-\frac{1}{T_o}$ brought by the smoothing filter of the external loop reference signal.

Since all the poles of the characteristic polynomial have negative real parts, the overall system is exponentially stable under the assumption that the reference signal $v_p^*$, the internal loop disturbance $f_i(t)$, and the external loop disturbance $f_o(t)$ are either constant or asymptotically tend toward constant values.

## 4. Results and discussion

To evaluate the performance and effectiveness of the proposed control approach, detailed time-domain simulations were carried out in MATLAB/Simulink for a Stacked Interleaved Buck Converter (SIBC) supplying a PEM electrolyzer. The simulations were executed using a fixed time step of $1 \times 10^{-6}$ s and a switching frequency of 20 kHz. The main electrical specifications of the SIBC and the controller parameters carefully tuned to ensure stable operation and fast dynamic response, are listed in Table 2.

In this section, the performance of the proposed *Active Disturbance Rejection Control (ADRC)* is compared with that of the *Second-Order Sliding Mode Control (SOSMC)*. The comparative study focuses on evaluating the transient and steady-state behavior, tracking accuracy, and robustness of both control strategies when applied to the *Stacked Interleaved Buck Converter (SIBC)* feeding a PEM electrolyzer. All simulations were performed under identical operating conditions, including converter parameters, reference profiles, and disturbance scenarios, to ensure a fair and objective comparison.

**Table 2**
Simulation parameters for SIBC, ADRC and SOSMC.

| Item | Components | Simulation value |
|---|---|---|
| SIBC | $E$ | 1000 V |
| | $C_p$ | 25 μF |
| | $C_s$ | 10 μF |
| | $L_p = L_s$ | 2 mH |
| | $R_p = R_s$ | 1 mΩ |
| ADRC | Outer loop | $T_i = 10^{-4}$ s, $\omega_i = 15\,000$ rad/s, $k_i = 12\,000$ |
| | Inner loop | $T_v = 10^{-3}$ s, $\omega_v = 9000$ rad/s, $k_v = 5000$ |
| SOSMC | Outer loop | $\beta_{SO1} = 500$, $c_{SO1} = 0.005$, $c_{SO2} = 2000$ |
| | Inner loop | $\beta_{SO2} = 1000$, $c_{SO3} = 8000$, $c_{SO4} = 5000$ |

### 4.1. Second-order sliding mode control (SOSMC)

The Second-Order Sliding Mode Control (SOSMC) strategy enhances the robustness properties of conventional Sliding Mode Control while significantly mitigating the chattering phenomenon through the use of a continuous control law derived from the Super-Twisting Algorithm (STA). This approach enables finite-time convergence of the system states and ensures improved dynamic tracking under parameter variations and external disturbances.

*Voltage loop.* The voltage control loop is designed using the sliding surface:

$$s_{SO1} = e_{SO1} + \beta_{SO1} \int e_{SO1}\, dt, \tag{55}$$

where $e_{SO1} = v_p - v_p^*$ denotes the voltage tracking error and $\beta_{SO1} > 0$ is the sliding surface coefficient.

The total control input is expressed as:

$$u = u_{eq} + u_{st}, \tag{56}$$

where $u_{eq}$ represents the equivalent control and $u_{st}$ the super-twisting correction term. By imposing the condition $\dot{s}_{SO1} = 0$, the equivalent control can be derived as:

$$u_{eq} = C_p \left( -\frac{i_s}{C_p} - \frac{-v_p + E_{rev} + V_{cath} + V_{anod}}{C_p R_{ohm}} + \dot{v}_p^* - \beta_{SO1} e_{SO1} \right). \tag{57}$$

The super-twisting term, which ensures finite-time convergence while reducing the chattering amplitude, is defined as:

$$u_{st} = C_p \left( -c_{SO1} |s_{SO1}|^{1/2} \operatorname{sgn}(s_{SO1}) - \int c_{SO2} \operatorname{sgn}(s_{SO1})\, dt \right), \tag{58}$$

where $c_{SO1}$ and $c_{SO2}$ are strictly positive design parameters.

*Current loop.* Similarly, the current control loop is governed by the sliding surface:

$$s_{SO2} = e_{SO2} + \beta_{SO2} \int e_{SO2}\, dt, \qquad e_{SO2} = i_p - i_p^*, \tag{59}$$

where $e_{SO2}$ denotes the current tracking error and $\beta_{SO2} > 0$ is a tuning coefficient.

Setting $\dot{s}_{SO2} = 0$ yields the equivalent control term:

$$u_{eq} = \frac{L_p}{E} \left( -\frac{R_p}{L_p} i_p - \frac{v_p}{L_p} + \frac{E}{L_p} - \dot{i}_p^* + \beta_{SO2} e_{SO2} \right). \tag{60}$$

The STA correction component is expressed as:

$$u_{st} = \frac{L_p}{E} \left( c_{SO3} |s_{SO2}|^{1/2} \operatorname{sgn}(s_{SO2}) + \int c_{SO4} \operatorname{sgn}(s_{SO2})\, dt \right), \tag{61}$$

where $c_{SO3}$ and $c_{SO4}$ are positive constants ensuring smooth convergence and robustness to uncertainties.

### 4.2. Comparative analysis of ADRC and SOSMC

To evaluate the dynamic performance and robustness of the two control strategies, several simulation tests were carried out under different operating conditions. Both controllers were implemented under the same converter and electrolyzer parameters to ensure a fair comparison.

The comparative study includes the following tests:

#### 4.2.1. Scenario 1 — Reference voltage variation

This test evaluates the ability of both controllers to follow different reference voltage levels. Under step changes of the reference, As shown in Fig. 6, the output reaches the new setpoint with a short settling time (10 ms), limited overshoot, and negligible steady-state error. The zoomed view confirms rapid stabilization without noticeable ringing. This is consistent with ADRC: the ESO compensates the lumped disturbance online, enabling a higher effective loop bandwidth without exciting overshoot, yielding a well-damped transient and high steady-state accuracy. Furthermore, as shown in Figs. 7, 8, 9 and 10, the estimated states by the Extended State Observer, namely $\hat{x}_{o1}$, $\hat{x}_{i1}$, $\hat{x}_{o2}$, and $\hat{x}_{i2}$, closely follow the actual signals, confirming the accuracy and responsiveness of the estimation process. These results demonstrate the robustness and effectiveness of the proposed control strategy in ensuring accurate reference tracking under dynamic conditions.

For Scenario 1, the ADRC control law (Fig. 11) remains nearly constant between reference changes, with smooth transitions, low high-frequency activity, and a well-bounded duty cycle. By contrast, the SOSMC control law (Fig. 12) exhibits a persistent oscillation about the equivalent control (chattering) even in steady state; at each reference step the transition is sharper and the transient ripple more pronounced. These observations, consistent with the output plots, indicate that both controllers achieve tracking, but ADRC provides a smoother and more economical actuation (hence potentially lower switching losses and ripple), whereas SOSMC is more aggressive and oscillatory.

#### 4.2.2. Scenario 2 — Input voltage disturbance

The second test investigates the system response under variations of the converter input voltage, which commonly occur in renewable energy systems such as PV or wind sources. As illustrated in Fig. 13 the output remains tightly regulated, showing bounded transient deviations and a quick recovery (10 ms) to the operating point. Peak deviations remain moderate. Since the ESO treats these fluctuations as a bounded, slowly time-varying disturbance, ADRC rejects them effectively as long as their dominant spectrum lies below the observer/control bandwidth, which explains the short recovery and small excursions observed. Regarding state estimation illustrated in Figs. 14, 15 and 17, good overall accuracy is observed for $\hat{x}_{o1}$, $\hat{x}_{i1}$, and $\hat{x}_{o2}$. However, the estimation of the internal disturbance $\hat{x}_{i2}$ presented in Fig. 16, associated with $f_i$, shows a discrepancy between the measured signal and the observer estimate emerges during the ∼30% input-voltage step. This transient stems from designing the current-loop observer at the nominal bus voltage ($E = 1000$ V); off-nominal operation introduces a model mismatch that temporarily increases the estimation error. Nevertheless, the control objectives (current and voltage loops) remain satisfied and the final setpoint is reached. Two practical levers can mitigate this: (i) use an adaptive or gain-scheduled observer with respect to $E$; (ii) inject the measured input voltage into the observer model, trading improved estimation accuracy for the added sensor and complexity.

For Scenario 2, the ADRC control law (Fig. 18) remains low and nearly piecewise-constant: at 0.5 s it shifts to a bounded plateau and then returns, with no sustained high-frequency oscillations, indicating effective disturbance rejection with limited control effort. By contrast, the SOSMC control law (Fig. 19) turns into a large-amplitude, high-frequency pulsating signal with near-boundary excursions; regulation is lost and the output no longer tracks the reference, entering a strongly oscillatory regime. In summary, ADRC maintains regulation with smooth, economical actuation, whereas SOSMC fails to maintain tracking and induces high switching activity and ripple.

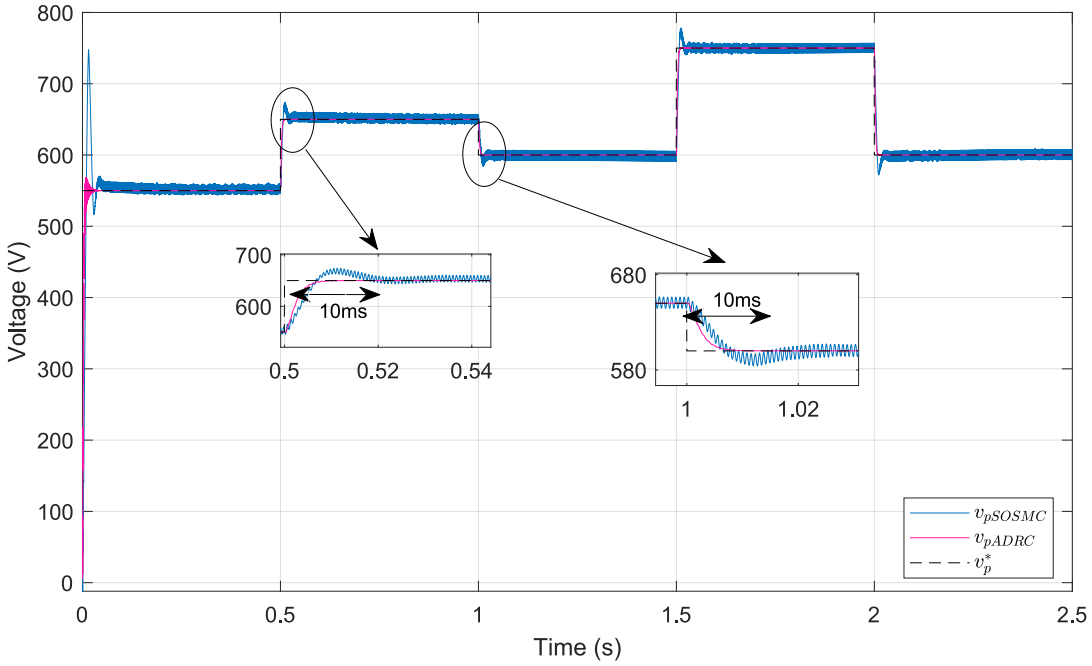


**Fig. 6.** Multi-Setpoint Output-Voltage Response: ADRC and SOSMC.

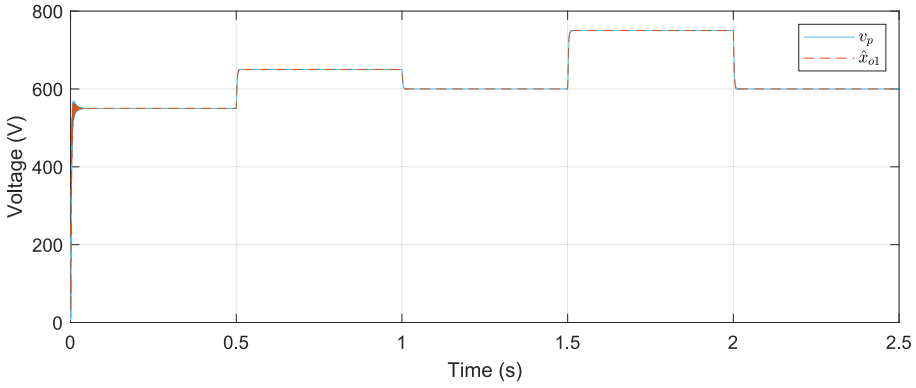


**Fig. 7.** Scenario 1: Voltage $v_p$ and its estimation $\hat{x}_{o1}$.

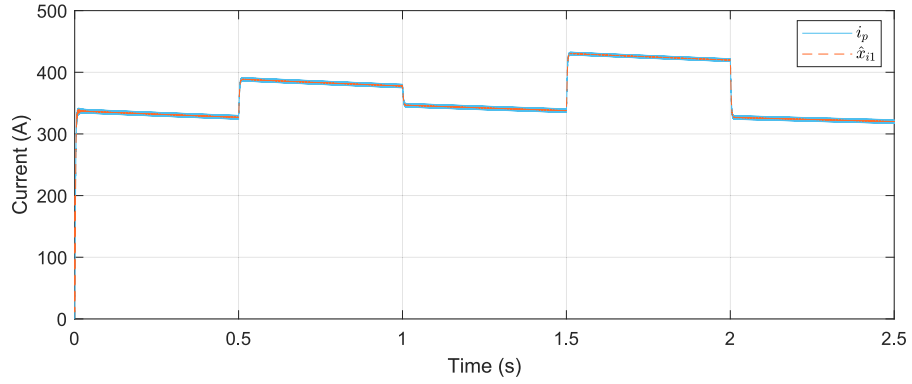


**Fig. 8.** Scenario 1: Current $i_p$ and its estimation $\hat{x}_{i1}$.

*4.2.3. Scenario 3 — Electrolyzer parameter variations*

This scenario aims to evaluate the robustness of the control strategy in response to internal variations in the electrolyzer's electrical parameters induced by a change in temperature. The double-layer capacitance is assumed to increase quasi-linearly with temperature due to enhanced ionic mobility at the electrode/electrolyte interface, as reported by Watzele et al. (2021). Meanwhile, the internal resistances of the system, including the membrane resistance $R_m$ and the activation resistances $R_a$ and $R_c$ are considered to decrease with temperature. This assumption is supported by the fact that higher temperatures improve

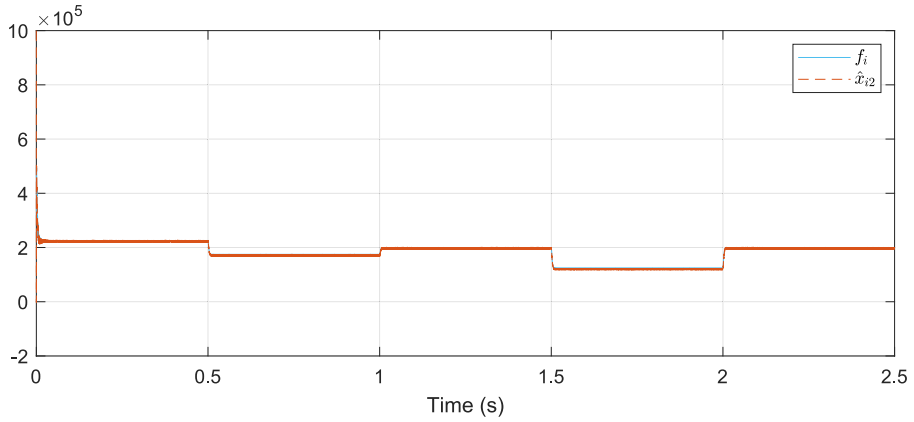


**Fig. 9.** Scenario 1: State variable $f_i$ and its estimation $\hat{x}_{i2}$.

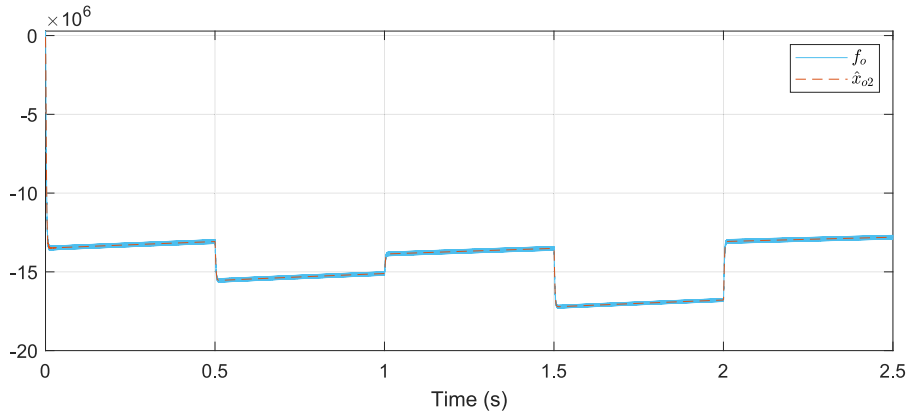


**Fig. 10.** Scenario 1: State variable $f_o$ and its estimation $\hat{x}_{o2}$.

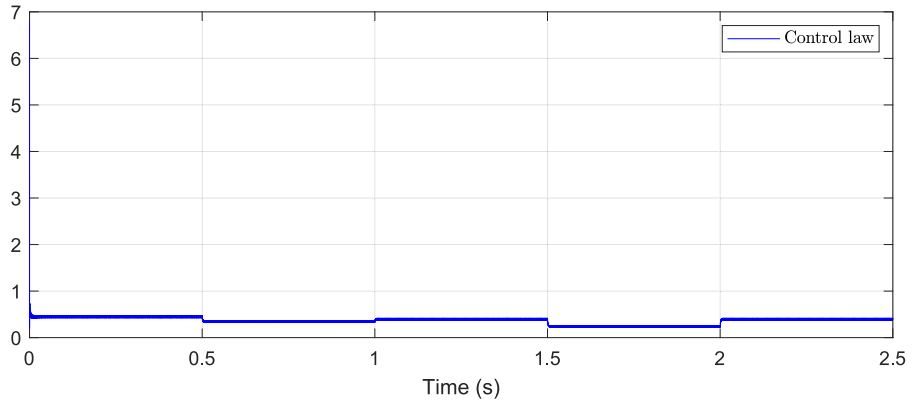


**Fig. 11.** Scenario 1: Control law of ADRC.

ionic conductivity and accelerate electrochemical reaction kinetics. This behavior is confirmed in Nafchi et al. (2022), who show that increasing the temperature significantly reduces resistive losses in PEM electrolyzers, thereby improving overall system efficiency.

As shown in Fig. 20 under parameter drifts, the ADRC-regulated output remains stable and quickly returns to the setpoint: the transient lasts $\approx$ 15 ms with a peak excursion of about 200 V, followed by negligible steady-state error. In contrast, SOSMC shows a pronounced loss of regulation around 0.5 s and, during the recovery at 1.0 s, a larger excursion 283 V with ringing before convergence. These observations confirm ADRC's robustnes to slow parameter variations: the ESO keeps the estimation error bounded and enables effective compensation, whereas SOSMC is more sensitive to model mismatch and rapid changes. Reported in Figs. 21–22–23, the estimations of $v_p$, $i_p$ and $f_i$ remain accurate even during dynamic phases. However, the estimations of $f_o$ provided in Fig. 24, exhibit slight deviations throughout the entire transition phases, indicating increased sensitivity of the observer under fast dynamic conditions.

Under Scenario 3, the ADRC control law (Fig. 25) remains low and nearly piecewise-constant; at the change instants it requires only short, bounded corrections, with no sustained high-frequency activity. By contrast, the SOSMC control law (Fig. 26) becomes markedly more aggressive, jumping toward the duty-cycle bounds and producing a high-frequency pulsating modulation with elevated switching activity. This contrast highlights the parsimonious actuation delivered by ADRC versus the near-boundary sliding action characteristic of SOSMC.

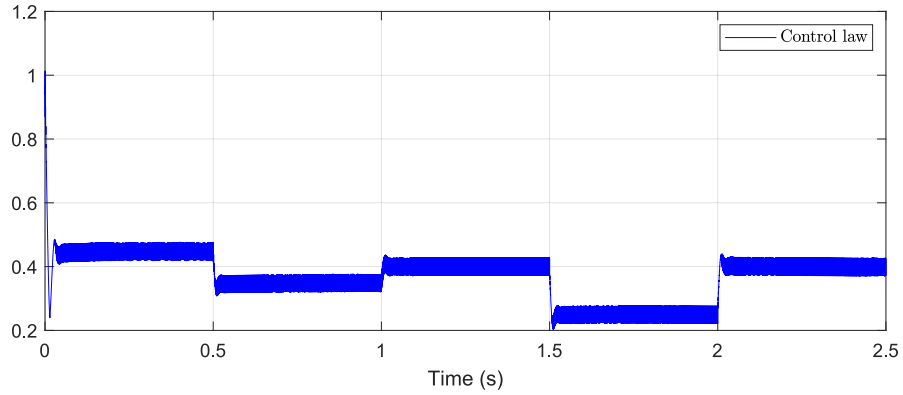


**Fig. 12.** Scenario 1: Control law of SOSMC.

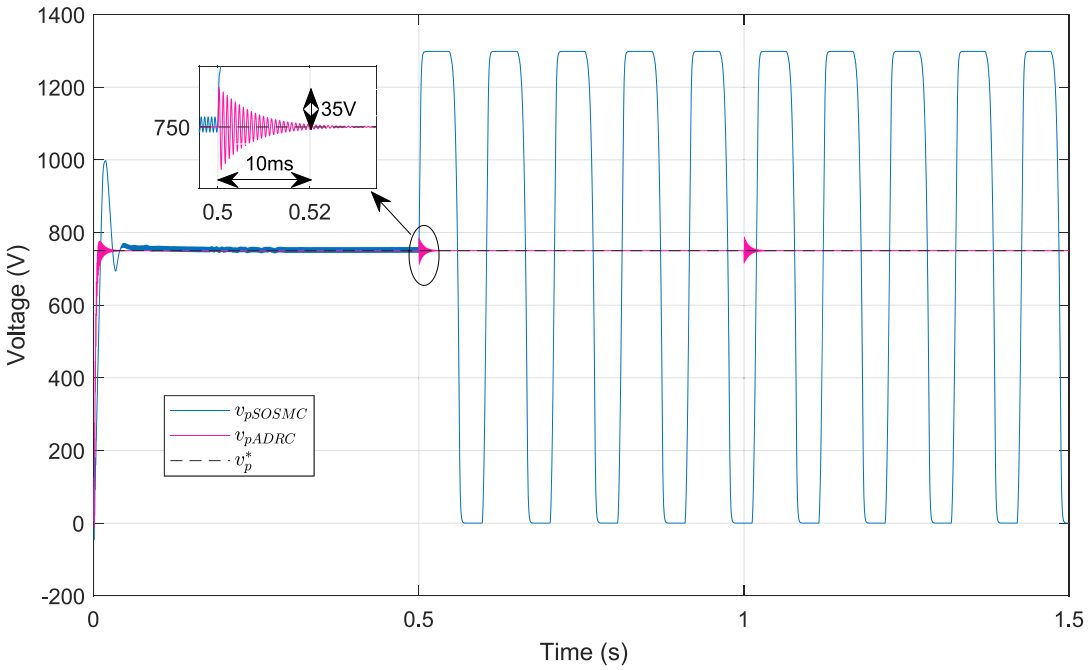


**Fig. 13.** Output Regulation Under Input-Bus Fluctuations: ADRC and SOSMC.

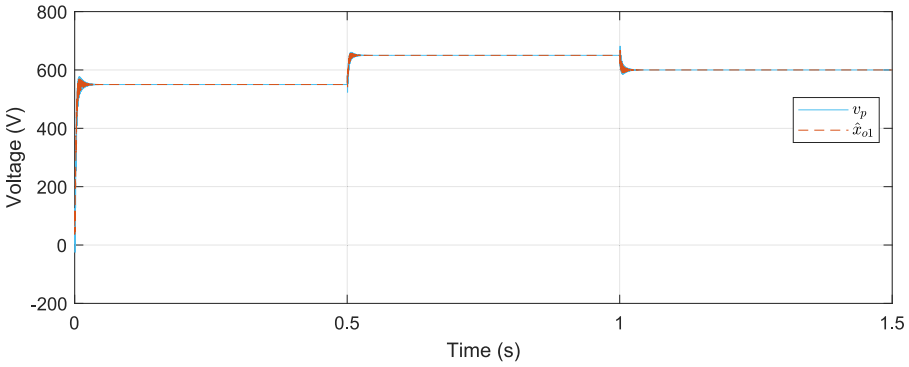


**Fig. 14.** Scenario 2: Voltage $v_p$ and its estimation $\hat{x}_{o1}$.

*4.2.4. Scenario 4 — Variation of the output capacitance $C_p$*

Finally, three additional simulations were performed with different values of the output capacitance $C_p$ to analyze the influence of this parameter on the converter dynamics. Starting from $C_p$ = 25 μF, the capacitance was increased successively to 50 μF, 75 μF, and 100 μF, as presented in Fig. 27. Under the output-capacitance sensitivity test,

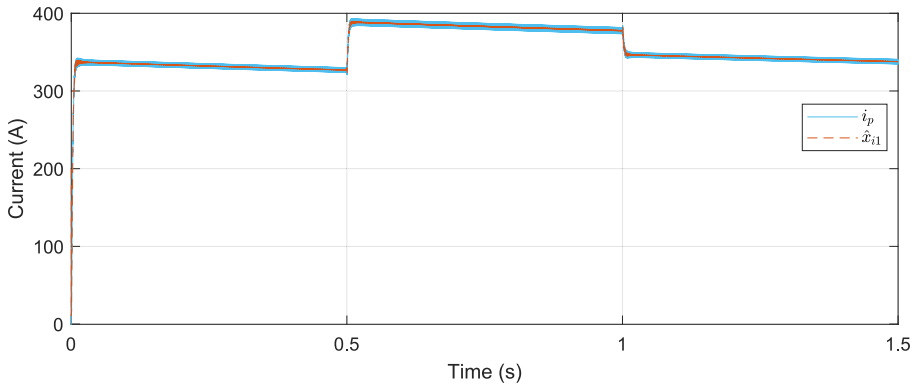


**Fig. 15.** Scenario 2: Current $i_p$ and its estimation $\hat{x}_{i1}$.

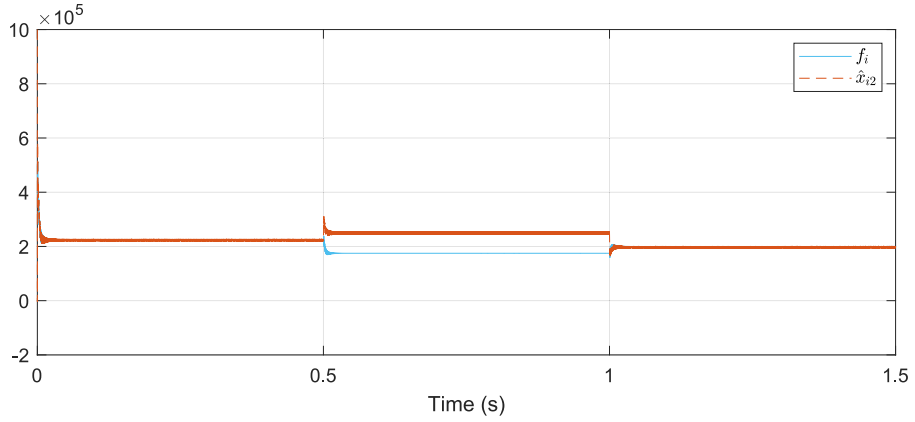


**Fig. 16.** Scenario 2: State variable $f_i$ and its estimation $\hat{x}_{i2}$.

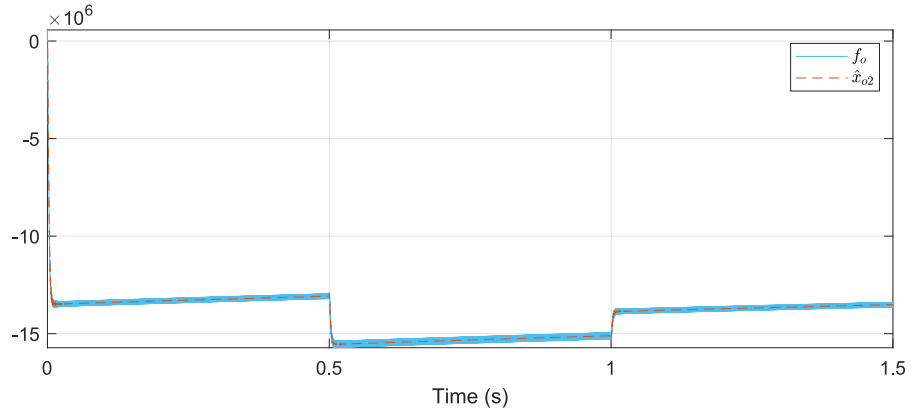


**Fig. 17.** Scenario 2: State variable $f_o$ and its estimation $\hat{x}_{o2}$.

the ADRC maintains a well-damped response, a rapid return to the setpoint, and negligible steady-state error, whereas SOSMC becomes progressively more oscillatory, with a growing oscillation envelope and longer decay time, approaching a loss of regulation at the largest $C_p$. These observations confirm ADRC's robust tuning against passive-component variations: ESO-based disturbance compensation and appropriate bandwidth placement preserve stability margins despite the pole shift induced by larger $C_p$, while SOSMC exhibits degraded damping and phase margin.

## 5. Discussion

The present work has been positioned within the context of recent research on control strategies for PEM electrolyzer converters. Several studies have addressed similar systems using advanced nonlinear or adaptive control techniques to enhance robustness, dynamic response, and efficiency under renewable-energy-induced fluctuations. Table 3 summarizes the main characteristics of these representative works, highlighting their scope, validation level, and key outcomes.

As shown in Table 3, most recent contributions have focused on sliding-mode or backstepping-based strategies, some incorporating adaptive or observer-based mechanisms. While these methods offer strong robustness, they often involve complex tuning or discontinuous control signals. In contrast, the dual-loop ADRC approach developed in this paper provides a simpler structure with comparable disturbance rejection and high tracking accuracy, as demonstrated through the comparative simulations against SOSMC (Section 4.2). Moreover, unlike

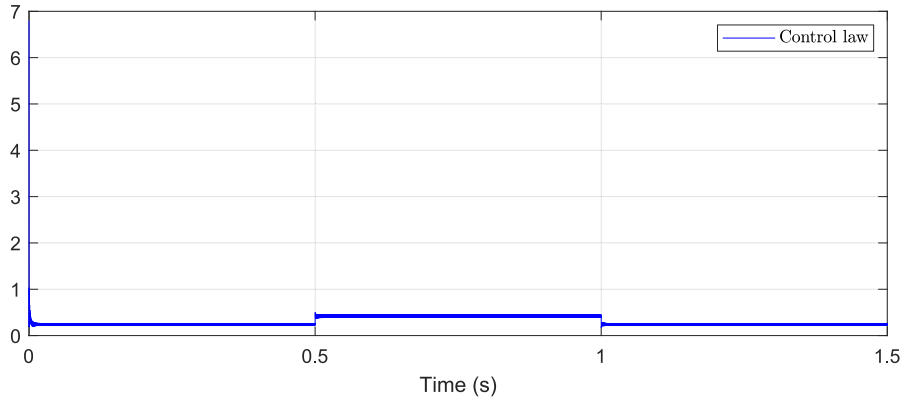


**Fig. 18.** Scenario 2: Control law of ADRC.

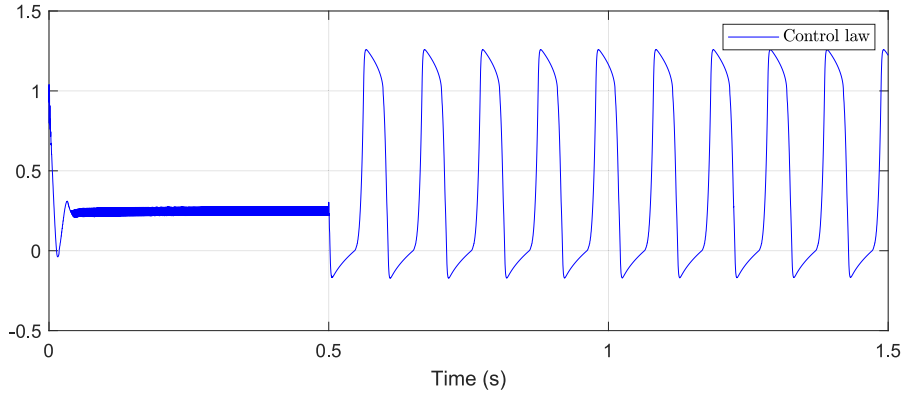


**Fig. 19.** Scenario 2: Control law of SOSMC.

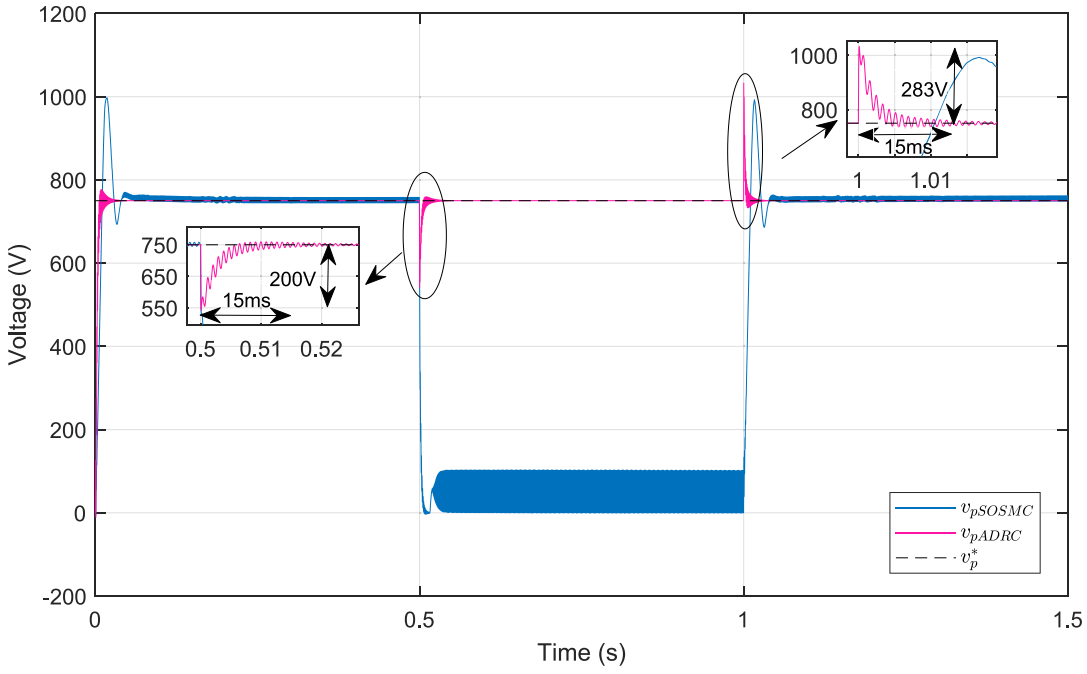


**Fig. 20.** Output-Voltage Response to Electrolyzer Parameter Variations: ADRC and SOSMC.

many previous studies limited to specific test cases, the present work investigates four representative operating scenarios: reference voltage variation, input voltage disturbance, electrolyzer parameter drift, and capacitance sensitivity.

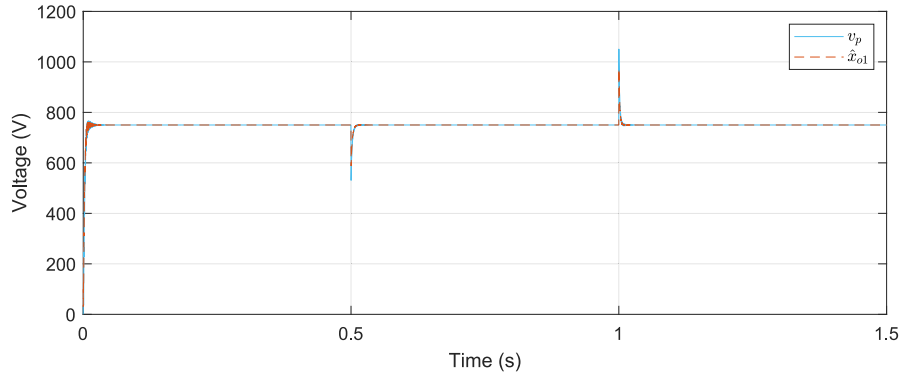


**Fig. 21.** Scenario 3: Voltage $v_p$ and its estimation $\hat{x}_{o1}$.

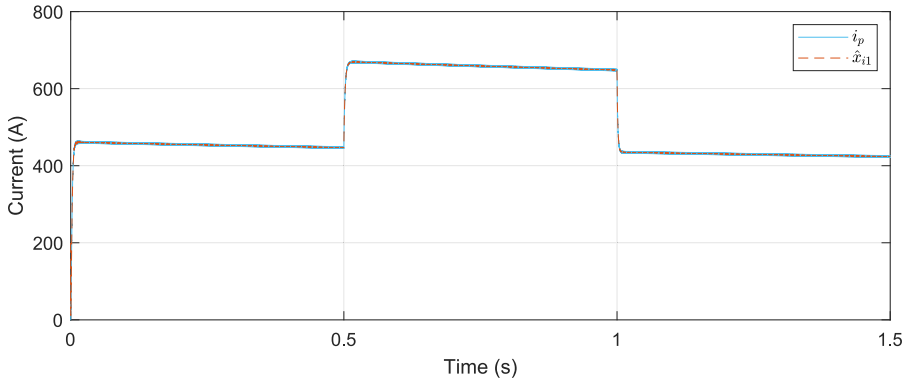


**Fig. 22.** Scenario 3: Current $i_p$ and its estimation $\hat{x}_{i1}$.

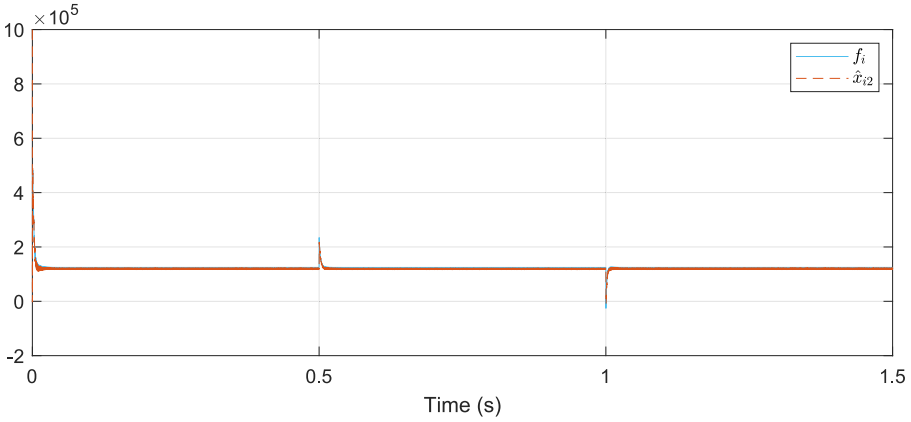


**Fig. 23.** Scenario 3: State variable $f_i$ and its estimation $\hat{x}_{i2}$.

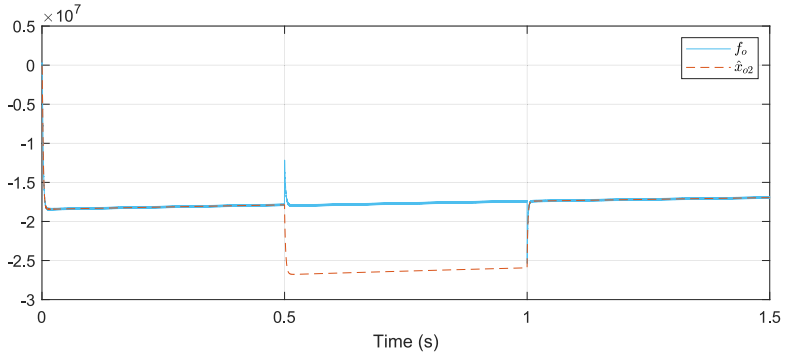


**Fig. 24.** Scenario 3: State variable $f_o$ and its estimation $\hat{x}_{o2}$.

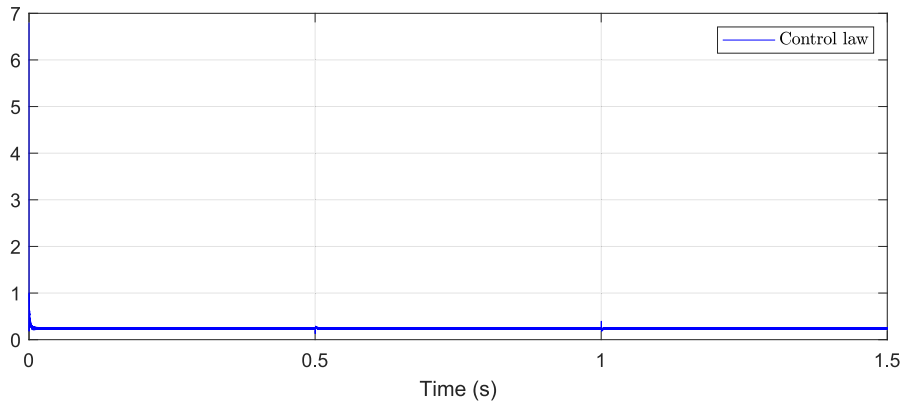


**Fig. 25.** Scenario 3: Control law of ADRC.

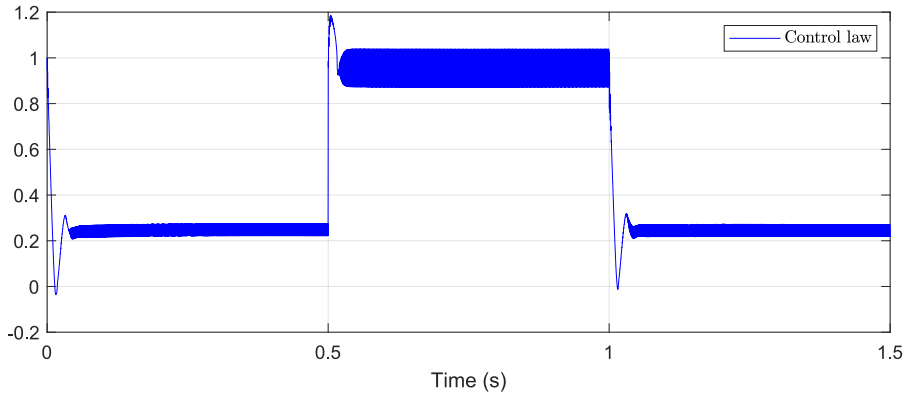


**Fig. 26.** Scenario 3: Control law of SOSMC.

**Table 3**
Summary of related works on PEM electrolyzer converters and control strategies.

| Study | Control strategy | Validation | Key focus/outcomes |
|---|---|---|---|
| (Makineni et al., 2025) SIBC–PEMEL | Integral SMC | Experiments (PEMEL emulator) | Faster dynamics; robust to input variations vs PI |
| (Yodwong et al., 2024) TLIBC–PEMEL | Improved nonlinear SMC | Experiments (PEMEL emulator) | Faster response; rise time set by controller; robust vs PI |
| (Koundi et al., 2022) IBC–PEMEL | Adaptive output-feedback ST–SMC + EKF | Simulations | Finite-time regulation; equal current sharing; handles parameter uncertainty |
| (Koundi et al., 2019) IBC–PEMEL | Output-feedback SMC + observer | Analysis + Simulations | Tight voltage regulation; asymptotic stability without measuring hidden states |
| (Baraean et al., 2024) Buck–PEMEL | PINN-aided adaptive backstepping TSMC | HIL | Fast settling (~0.025 s), limited overshoot (~17.5%), robust vs improved SMC |
| **This paper** | **Dual-loop ADRC** | **Simulations** | **Formal stability; benchmark vs SOSMC; scenarios: ref/input/params/$C_p$** |

**Table 4**
Tracking performance under multiple reference setpoints.

| Controller | Settling time (ms) | Undershoot (%) | Overshoot (%) | Steady-state error (%) |
|---|---|---|---|---|
| ADRC | 10 | 0 | 20.06 | 0.05 |
| SOSMC | 80 | 1.99 | 30 | 0.98 |

Overall, this study complements previous research by providing a stability-guaranteed and practically implementable solution for renewable-powered hydrogen production systems.

To anchor the discussion in quantitative evidence, Table 4 summarizes tracking performance under multiple reference setpoints. With the corrected figures, ADRC achieves a shorter settling time (10 ms versus 80 ms), zero undershoot (0% versus 1.99%), a lower overshoot (20.06% versus 30%), and a smaller steady-state error (0.05% versus 0.98%) than SOSMC. This indicates that, on a nominal multi-step tracking task, ADRC delivers both faster and tighter regulation. These quantitative results complement the time-domain evidence in the other scenarios (input-voltage disturbance, electrolyzer-parameter drift, and output-capacitance variation), where the figures already show ADRC

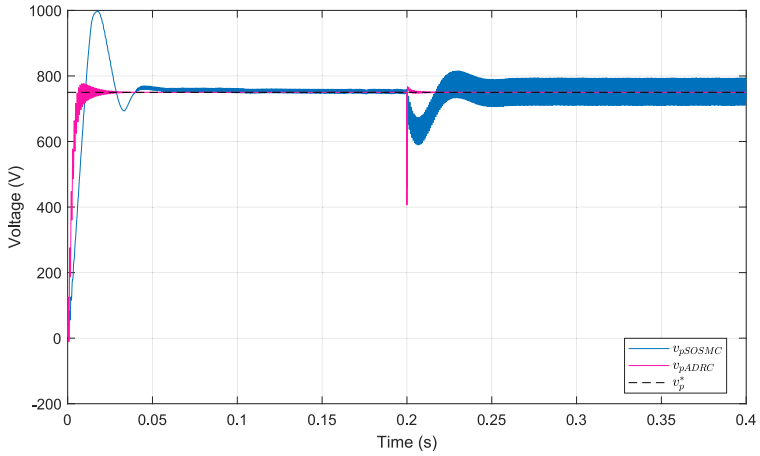


(a) Case 1

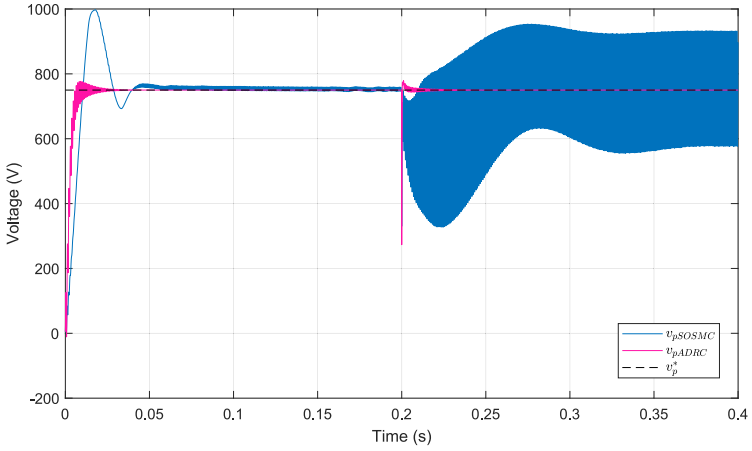


(b) Case 2

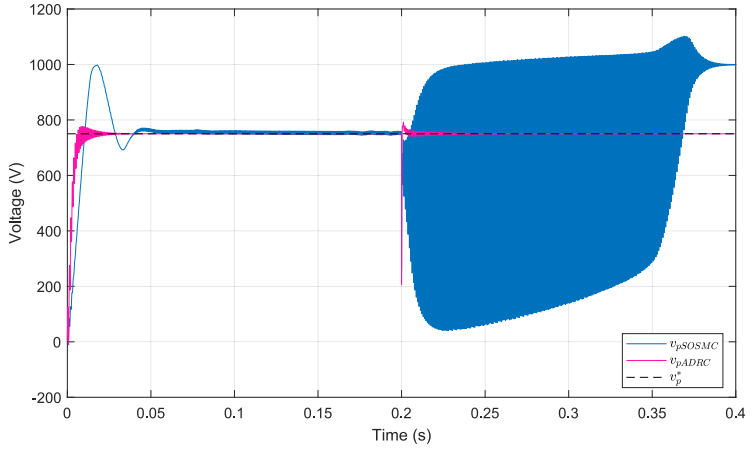


(c) Case 3

**Fig. 27.** Output-voltage response to output-capacitance $C_p$ variation: Case 1: $C_p = 50\,\mu F$; Case 2: $C_p = 75\,\mu F$; Case 3: $C_p = 100\,\mu F$.

maintaining stable operation with reduced oscillations and reliable recovery.

## 6. Conclusion

In this study, a dual-loop control strategy based on Active Disturbance Rejection Control (ADRC) was developed for a parallel interleaved buck converter supplying a PEM electrolyzer. The method ensures output-voltage regulation under external disturbances and internal uncertainties (including temperature-driven parameter drifts) and is supported by a rigorous modeling framework that integrates the electrolyzer's static and dynamic behavior with converter dynamics, together with a closed-loop stability analysis. Quantitatively, under multiple setpoints ADRC outperforms SOSMC with a settling time of 10 ms versus 80 ms, undershoot of 0% versus 1.99%, overshoot of 20.06% versus 30%, and steady-state error of 0.05% versus 0.98%. ADRC also recovers quickly from input-bus disturbances (≈10 ms) and,

under electrolyzer parameter variations, limits the peak excursion to ≈200 V (SOSMC ≈283 V) with ≈15 ms recovery, maintaining stable operation without sustained ringing across output-capacitance changes (50–100 μF). Future research will explore the development of adaptive or learning-based observers tailored for electrolyzers with drifting parameters, the scaling of ADRC strategies to multi-converter and large-scale PEM systems, and the integration of the proposed control method with experimental verification and hardware-in-the-loop testing.

## CRediT authorship contribution statement

**Nada Chhab:** Writing – original draft, Validation, Software, Resources, Methodology, Conceptualization. **Abdelmajid Abouloifa:** Writing – review & editing, Validation, Supervision, Project administration, Methodology, Funding acquisition, Conceptualization. **Elhoussin Elbouchikhi:** Writing – review & editing, Validation, Supervision, Project administration, Methodology, Funding acquisition, Conceptualization. **Azeddine Houari:** Writing – review & editing, Validation, Supervision, Methodology, Conceptualization. **Ibtissam Lachkar:** Writing – review & editing, Validation, Supervision, Methodology, Conceptualization.

## Declaration of Generative AI and AI-assisted technologies in the writing process

During the preparation of this work the authors used ChatGPT in order to improve the grammar and readability of some sentences. After using these tools/services, the authors reviewed and edited the content as needed and take full responsibility for the content of the publication.

## Declaration of competing interest

The authors declare that they have no known competing financial interests or personal relationships that could have appeared to influence the work reported in this paper.

## Acknowledgment

The authors acknowledge the financial support from ISEN Yncréa Ouest, Nantes and PHC Toubkal under grant number N°: TBK/24/185-Campus France: 49960SJ. With the support of the CNRST as part of the ”PhD-ASsociate Scholarship – PASS” Program. All authors have read and approved the final version of the manuscript.

## Data availability

No data was used for the research described in the article.

## References

Abdel-Rahim, O., et al., 2024. Enhancing hydrogen generation through advanced power conditioning. Energy Rep. 12, 775–786. http://dx.doi.org/10.1016/j.egyr.2024.06.049.

Al-Obaidi, N.A., et al., 2022. A review of non-isolated bidirectional DC–DC converters. In: IICETA 2022. http://dx.doi.org/10.1109/IICETA54559.2022.9888704.

Baraean, A., et al., 2024. Physics-informed NN-based adaptive control of buck converter for PEM electrolyzer. Heliyon 10, e29254. http://dx.doi.org/10.1016/j.heliyon.2024.e29254.

Bovo, A., et al., 2023. Hydrogen energy storage system in a multi-technology microgrid. Int. J. Hydrog. Energy 48, 12072–12088. http://dx.doi.org/10.1016/j.ijhydene.2022.11.346.

Cao, Y., et al., 2020. Efficient terminal voltage control for PEMFC. Energy Rep. 6, 530–542. http://dx.doi.org/10.1016/j.egyr.2020.02.035.

Castañeda, L.A., Luviano-Juárez, A., Chairez, I., 2015. Robust trajectory tracking of a delta robot through adaptive active disturbance rejection control. IEEE Trans. Control Syst. Technol. 23, 1387–1398. http://dx.doi.org/10.1109/TCST.2014.2367313.

Concha, D., et al., 2024. Interleaved dual buck converter for low-carbon hydrogen production: electrolyzer current control and input capacitors voltage balancing. In: IECON 2024. http://dx.doi.org/10.1109/IECON55916.2024.10905714.

Elalfy, D.A., et al., 2024. Comprehensive review of energy storage systems technologies. Energy Strat. Rev. 54, 101482. http://dx.doi.org/10.1016/j.esr.2024.101482.

Farooq, A., et al., 2015. A review of non-isolated high step-down DC–DC converters. Int. J. Smart Home 9, 133–150. http://dx.doi.org/10.14257/ijsh.2015.9.8.15.

Franco, A., Giovannini, C., 2023. Recent and future advances in water electrolysis for green hydrogen generation. Sustainability 15, 16917. http://dx.doi.org/10.3390/su152416917.

Gao, Z., 2003. Scaling and bandwidth-parameterization based controller tuning. In: Proceedings of the American Control Conference. pp. 4989–4996. http://dx.doi.org/10.1109/ACC.2003.1242516.

Gao, Z., 2006. Active disturbance rejection control: a paradigm shift in feedback control system design. In: Proceedings of the American Control Conference. http://dx.doi.org/10.1109/ACC.2006.1656579.

Greco, N., et al., 2017. A 100-mw fully integrated DC–DC converter with double galvanic isolation. In: ESSCIRC 2017. http://dx.doi.org/10.1109/ESSCIRC.2017.8094583.

Guida, V., et al., 2018. Candidate interleaved DC–DC buck converters for electrolyzers. In: EEEIC 2018. http://dx.doi.org/10.1109/EEEIC.2018.8494457.

Guilbert, D., Vitale, G., 2021. Hydrogen as a clean and sustainable energy vector for global transition from fossil-based to zero-carbon. Clean Technol. 3 (4), 881–909. http://dx.doi.org/10.3390/cleantechnol3040051.

Guo, X., Zhang, S., Liu, Z., Sun, L., Lu, Z., Hua, C., Guerrero, J.M., 2022. A new multi-mode fault-tolerant operation control strategy of multiphase stacked interleaved buck converter for green hydrogen production. Int. J. Hydrog. Energy 47, 30359–30370. http://dx.doi.org/10.1016/j.ijhydene.2022.06.249.

Han, J., 2009. From PID to active disturbance rejection control. IEEE Trans. Ind. Electron. 56 (3), 900–906. http://dx.doi.org/10.1109/TIE.2008.2011621.

Khalid, M., 2024. Smart grids and renewable energy systems. Energy Strat. Rev. 51, 101299. http://dx.doi.org/10.1016/j.esr.2024.101299.

Koundi, M., et al., 2019. Output feedback sliding mode control of PEM EL-IBC system. IFAC-PapersOnLine 52, 85–90. http://dx.doi.org/10.1016/j.ifacol.2019.12.626.

Koundi, M., et al., 2022. Hydrogen flow rate control using adaptive output feedback sliding mode. IFAC-PapersOnLine 55, 282–287. http://dx.doi.org/10.1016/j.ifacol.2022.07.325.

Koundi, M., et al., 2023. Investigation of hydrogen production system based PEM EL. Clean Technol. 5, 531–568. http://dx.doi.org/10.3390/cleantechnol5020028.

Kumar, S. Shiva, Himabindu, V., 2019. Hydrogen production by PEM water electrolysis – a review. Mater. Sci. Energy Technol. 2, 442–454. http://dx.doi.org/10.1016/j.mset.2019.03.002.

Kumar, V., Nagendrappa, H., 2023. Four-phase interleaved bidirectional DC–DC converter for battery energy storage system. In: Proc. 2023 7th International Conference on Computer Applications in Electrical Engineering. CERA, pp. 1–6. http://dx.doi.org/10.1109/CERA59325.2023.10455518.

Li, J., Xia, Y., Qi, X., Gao, Z., 2017. On the necessity, scheme, and basis of the linear–nonlinear switching in active disturbance rejection control. IEEE Trans. Ind. Electron. 64, 1425–1435. http://dx.doi.org/10.1109/TIE.2016.2611573.

Ma, R., Xu, L., Xie, R., Zhao, D., Huangfu, Y., Gao, F., 2019. Advanced robustness control of DC–DC converter for proton exchange membrane fuel cell applications. IEEE Trans. Ind. Appl. 55, 6389–6400. http://dx.doi.org/10.1109/TIA.2019.2935981.

Makineni, R.R., et al., 2025. Integral sliding mode control of a stacked interleaved buck converter. IEEE Trans. Ind. Appl. 61, 450–462. http://dx.doi.org/10.1109/TIA.2024.3477414.

Marefatjouikilevaee, H., et al., 2023. Static and dynamic electrical models of PEM electrolysers. Energies 16, 6503. http://dx.doi.org/10.3390/en16186503.

Marish Kumar, P., Priya, N., Dhilipkumar, R., Santhana Krishnan, T., 2024. Maximizing solar energy efficiency with efficient interleaved boost converter with three-level neutral point clamped inverter for grid-connected photovoltaic using hybrid approach. Sol. Energy 280, 112855. http://dx.doi.org/10.1016/j.solener.2024.112855.

Melo, R.R. De, Tofoli, F.L., Daher, S., Antunes, F.L.M., 2020. Interleaved bidirectional DC–DC converter for electric vehicle applications based on multiple energy storage devices. Electr. Eng. 102, 2011–2023. http://dx.doi.org/10.1007/s00202-020-01009-3.

Mumtaz, F., et al., 2021. Review on non-isolated DC–DC converters. Ain Shams Eng. J. 12, 3747–3763. http://dx.doi.org/10.1016/j.asej.2021.03.022.

Nafchi, F. Moradi, et al., 2022. Thermal and electrochemical analyses of a PEM electrolyzer. Int. J. Hydrog. Energy 47, 40172–40183. http://dx.doi.org/10.1016/j.ijhydene.2022.05.069.

Nnabuife, S.G., et al., 2025. Integration of renewable energy sources with electrolysis. Int. J. Hydrog. Energy 107, 218–240. http://dx.doi.org/10.1016/j.ijhydene.2024.06.342.

Ram, M., et al., 2022. Global energy transition to 100% renewables by 2050. Energy 246, 123419. http://dx.doi.org/10.1016/j.energy.2022.123419.

Ratib, M.K., et al., 2025. Large-scale production of green hydrogen from solar energy. Int. J. Hydrog. Energy 98, 873–886. http://dx.doi.org/10.1016/j.ijhydene.2024.10.281.

Shen, S., Xu, J., 2021. Adaptive neural network-based active disturbance rejection flight control of an unmanned helicopter. Aerosp. Sci. Technol. 119, 107062. http://dx.doi.org/10.1016/j.ast.2021.107062.

Sun, L., Hua, Q., Shen, J., Xue, Y., Li, D., Lee, K.Y., 2017. Multi-objective optimization for advanced superheater steam temperature control in a 300 MW power plant. Appl. Energy 208, 592–606. http://dx.doi.org/10.1016/j.apenergy.2017.09.095.

Wang, D., et al., 2023. Adaptive linear ADRC method for HVDC transmission system. Energy Rep. 9, 3282–3289. http://dx.doi.org/10.1016/j.egyr.2023.02.001.

Watzele, S.A., et al., 2021. Temperature dependences of the double layer capacitance. Electrochim. Acta 391, 138969. http://dx.doi.org/10.1016/j.electacta.2021.138969.

Wu, Y., Wang, L., Zhang, J., Li, F., 2019. Path following control of autonomous ground vehicle based on nonsingular terminal sliding mode and active disturbance rejection control. IEEE Trans. Veh. Technol. 68, 6379–6390. http://dx.doi.org/10.1109/TVT.2019.2916982.

Yang, Y., et al., 2024. Energy transition: connotations, mechanisms and effects. Energy Strat. Rev. 52, 101320. http://dx.doi.org/10.1016/j.esr.2024.101320.

Yodwong, B., et al., 2023. Open-circuit switch fault diagnosis and accommodation of a three-level interleaved buck converter for electrolyzer applications. Electronics 12, 1349. http://dx.doi.org/10.3390/electronics12061349.

Yodwong, B., et al., 2024. Improved sliding mode-based controller of a high voltage ratio DC–DC converter. IEEE Trans. Ind. Electron. 71, 8831–8840. http://dx.doi.org/10.1109/TIE.2023.3322009.

Yue, M., et al., 2021. Hydrogen energy systems: a critical review. Renew. Sustain. Energy Rev. 146, 111180. http://dx.doi.org/10.1016/j.rser.2021.111180.

Zhang, D., Wu, Q., Yao, X., 2018. Bandwidth based stability analysis of ADRC. J. Syst. Sci. Complex. 31, 1449–1468. http://dx.doi.org/10.1007/s11424-018-7073-4.

Zhao, W., Nielsen, M.R., Kjær, M., Iov, F., Nielsen, S.M., 2023. Grid integration of a 500 kw alkaline electrolyzer system for harmonic analysis and robust control. E-Prime 5, 100217. http://dx.doi.org/10.1016/j.prime.2023.100217.

Zhou, W., Shao, S., Gao, Z., 2009. A stability study of ADRC by a singular perturbation approach. Appl. Math. Sci. 3, 491–508.